Regional-Scale Chemical Transport Modeling in Support of Intensive Field Experiments: Overview and Analysis of the TRACE-P Observations

G.R. Carmichael[1], Y. Tang[1], G. Kurata[3], I. Uno[2], D.G. Streets[4], J-H Woo[1], H. Huang[1], J. Yienger[1], B. Lefer[5], R.E. Shetter[5], D.R. Blake[6], E. Atlas[5], A. Fried[5], E. Apel[5], F. Eisele[5], C. Cantrell[5], M.A. Avery[7], J.D. Barrick[7], G.W. Sachse[7], W.L. Brune[8], S.T. Sandholm[9], Y. Kondo[10], H.B. Singh[11], R.W. Talbot[12], A. Bandy[13], D. Thorton[13], A.D. Clarke[14], and B.G. Heikes[15]

[1] Center for Global and Regional Environmental Research, University of Iowa, Iowa, USA
[2] Research Institute for Applied Mechanics, Kyushu University, Fukuoka, Japan
[3] Department of Ecological Engineering, Toyohashi University of Technology, Toyohashi, Japan
[4] Decision and Information Sciences Division, Argonne National Laboratory, Argonne, IL, USA
[5] National Center for Atmospheric Research, Colorado, USA
[6] Department of Chemistry, University of California at Irvine, California, USA
[7] NASA Langley Center, Virginia, USA
[8] Department of Meteorology, Pennsylvania State University, Pennsylvania, USA
[9] Georgia Institute of Technology, Georgia, USA
[10] Research Center for Advanced Science and Technology, University of Tokyo, Tokyo, Japan
[11] NASA Ames Research Center, California, USA
[12] Institute for the Study of Earth, Oceans, and Space, University of New Hampshire, New Hampshire, USA
[13] Chemistry Department, Drexel University, Pennsylvania, USA
[14] School of Ocean and Earth Science and Technology, University of Hawaii, Hawaii, USA
[15] Graduate School of Oceanography, University of Rhode Island, Rhode Island, USA

Abstract

The CFORS/STEM-2K1, regional-scale, chemical transport model is used in the analysis of the aircraft data obtained during the TRACE-P experiment. Calculated trace gas and aerosol distributions are presented and compared to the *in-situ* data. The regional model is shown to accurately predict many of the important features observed. When compared to all 5-minute averaged ethane measurements, 80% of the model calculated values fall within +/- 30% of the observed values, and 86% of the data is captured to within a factor of 2. When all the modeled parameters are analyzed it is found that the meteorological parameters are modeled most accurately, reflecting the large amount of observational data ingested into the reanalysis of the large-scale meteorological fields. The model is shown to explain between 35 to 70% of the observed variability in a wide variety of trace species. Case studies of frontal outflow and transport into the Yellow Sea are presented and illustrate the complex nature of outflow. Biomass burning from SE Asia is often transported in the warm conveyor belt at altitudes above ~2 km and at latitudes below 30N. Outflow of pollution emitted along the east coast of China in the post-frontal regions is typically confined to the lower ~2 km and results in high concentrations with plume-like features in the Yellow Sea. During these situations the model under predicts CO and black carbon (among other species). While clearly more work is needed to improve the inventories, results presented here show that the emissions inventories are of sufficient quality to support preliminary studies of ozone production. Analysis of the springtime ozone production in East Asia and its sensitivity to NO_x and NMHC levels are presented.

INDEX TERMS: 0305 Aerosols and particles; 0322 Constituent sources and sinks; 0345 Pollution—urban and regional; 0365 Troposphere—composition and chemistry

1. Introduction

Chemical Transport Models (CTMs) are playing increasingly important roles in the design, execution, and analysis of large-scale atmospheric chemistry field studies. They are being used in forecast-mode to enhance flight planning by enabling the representation of important three-dimensional atmospheric chemical structures (such as dust storm plumes, polluted air masses associated with large cities, and widespread biomass burning events) and how they evolve over time. CTM forecasts play the additional important role of providing a 4-dimensional contextual representation of the experiment. CTMs also facilitate the integration of the different measurements and measurement platforms (e.g., aircraft, ground stations and satellite observations). Finally, CTMs can be used to help evaluate and improve emission estimates.

We developed an operational regional-scale forecasting and analysis system to assist in atmospheric field experiments. The Chemical weather FORecasting System (CFORS) consists of 3 major components: 1) detailed mesoscale meteorological model with on-line air mass and emission tracers; 2) detailed 3-dimensional photochemical calculations using CTMs; and 3) an emissions module that intimately links emitted amounts and activities to the transport and chemistry analysis. CFORS was applied in the design and execution of the NASA TRACE-P, NSF ACE-Asia and the NOAA ITCT-Y2K2 intensive field experiments. In this paper we present a brief overview of the CFORS system, and focus on the use of the STEM-2K1 CTM in the analysis of the TRACE-P observations.

2. Model Description

An overview of the CFORS/STEM-2K1 modeling system as used in TRACE-P and ACE-Asia experiments is shown in **Figure 1**. CFORS is a multi-tracer, on-line, system built within the RAMS mesoscale meteorological model (*Pielke et al., 1992*). A unique feature of CFORS is that multiple tracers are run on-line in RAMS, so that all the on-line meteorological information such as 3-D winds, boundary-layer turbulence, surface fluxes and precipitation

amount are directly used by the tracer model at every time step. As a result, CFORS produces with high time resolution 3-dimensional fields of tracer distributions and major meteorological parameters. CFORS includes a wide variety of tracers to help characterize air masses. These include: 1) important anthropogenic species (SO_2/SO_4, CO, black carbon, organic carbon, fast and slow reacting hydrocarbons, and NO_x); 2) species of natural origin (yellow sand, sea salt, radon, volcanic SO_2); and 3) markers for biomass burning (CO, black carbon, and organic carbon) and megacities. CFORS on-line forecast products consist of gas and aerosol mass distributions, and meteorological parameters. The numerical model domain of CFORS-on-line, is centered at 25°N 115°E with a horizontal grid of 100 by 90 grid points and a resolution of 80 km. In the vertical, the domain is divided into 23 layers, with the top level at 23km.

CFORS can be operated both in forecast and hind cast modes. During the TRACE-P and ACE-Asia intensive observations, CFORS was run in an operational forecasting mode and provided daily forecasts of meteorology and gas/aerosol distributions. A unique element of the operational model was that two separate forecasts were produced each day; one where the RAMS model was initialized by the NCEP (National Center for Environmental Prediction/ NOAA) 96 hour forecasting AVN data set (http://www.emc.ncep.noaa.gov/modelinfo/index.html); and the second using JMA (Japan Meteorological Agency) 72 hour forecasting ASIA domain data set (http://ddb.kishou.go.jp/). Both NCEP and JMA forecasting results were also used for RAMS nudging calculations. This procedure provided some measure of the forecast variability. For each day the following 72-hr forecasts were provided: 1) CFORS/on-line produced meteorological and tracer fields for both JMA and NCEP initializations; 2) photochemical fields using the RAMS fields to drive STEM-2K1 at 80 km; and 3) same as 2) but for 16 km horizontal resolution. After the field campaigns, the CFORS system was applied in hind cast mode using ECMWF global meteorological data set (6 hour interval with 1°×1° resolution), analyzed weekly SST (sea surface temperature) data, and observed monthly snow-cover information as the boundary conditions for the RAMS calculations. All calculations were performed on Linux clusters and results were made available via the CFORS web manager. The CGI interactive interface can plot 2-D of fields and time-height cross-sections at fixed points according to user's requests. Quick-look vis5D 3-D animations were also provided. The CFORS web site can be accessed at

http://cfors.riam.kyushu-u.ac.jp/~cforsdemo/index.html. Further details regarding the CFORS/on-line are presented in *Uno et al.,* (2002).

The meteorological fields, and those emissions estimated in an on-line manner inside of CFORS, were used to drive the STEM-2K1 comprehensive CTM, which then produced estimated fields of primary and secondary chemical and aerosol constituents. This model is an enhanced version of the STEM model, which has been used in a series of studies that include: (1) the modeling of dust transport in East Asia and the interactions of the trace gas species with mineral aerosols for the period of May 1987 (*Phadnis*, 1999; *Phadnis and Carmichael*, 2000; *Xiao et al*., 1997); (2) simulation of smoke associated with a forest fire episode in Northern China for the month of May 1987 (*Phadnis and Carmichael*, 2000a); (3) process simulations to better understand aerosol-chemistry interactions including partitioning of nitric acid and direct ozone reactions and renoxification reactions on aerosol surfaces (*Zhang and Carmichael*, 1999; *Song and Carmichael*, 1999a); and (4) simulations of sea salt and mineral aerosol during the PEM-West B period to study processes influencing the aging of aerosols in east Asia (*Song*, 1999; *Song and Carmichael*, 2001); *Underwood et al*., (2001).

The important new features in STEM-2K1 include: i) the use of the SAPRC99 chemical mechanism (*Carter 2000*), which consists of 93 species and 225 reactions; ii) the integration of the chemical mechanism using and the implicit second order Rosenbrock method (*Verwer et al 1997*); iii) the calculation of photolysis rates on-line, considering the influences of cloud, aerosol and gas-phase absorptions due to O_3, SO_2 and NO_2, using the NCAR Tropospheric Ultraviolet-Visible (TUV) radiation model (*Madronich, 1999*); and iv) the extension of the aerosol calculations to include optical information (e.g., extinction) in addition to mass, size and composition. Details regarding the radiative transfer calculations are presented in *Tang et al., (this issue, a)*. Boundary conditions were selected based on observational data. In general values were taken as the lowest 5% at each altitude of the values observed during TRACE-P.

An important aspect of the CFORS system is that emissions development and analysis are intimately coupled to the modeling activities. The anthropogenic emission inventories (SO_x, NO_x, CO, CO_2, NH_3, Black Carbon, Organic Carbon and Hydrocarbons) were prepared

specifically for the TRACE-P and ACE-Asia experiments and were based on year 2000 grided annual emission. A unique aspect of this bottoms-up inventory is that it is driven by regional-specific information on fuels and activity. Biofuels and fossil fuels can be tracked separately, as can emissions from various economic sectors (e.g., domestic, transport, power generation, industrial). Emissions from specific regions and even megacities can be isolated. The details of the inventory are presented in *Streets et al.,* and *Woo et al.,* (this issue).

Natural gaseous (i.e., radon and lightning NO_x) and aerosol sources (dust and sea salt) are calculated on-line in CFORS. CFORS treats size-resolved mineral dust using 12 particle bins (ranging from 0.1 to 20 μm in radius). In CFORS the dust emissions are calculated on-line using a vertical dust deflatation scheme as a power law function of surface friction velocity u_* (e.g., *Gillette and Passi*, 1988). Further details pertaining to the dust emission technique are presented in *Uno et al.* (2001). Lighting NO_x is included as a tracer to provide estimates of air masses impacted by lightning. Lightning NO_x emissions are calculated on-line based on estimates of subgrid scale cumulus activity calculated by a simplified Kuo cumulus scheme. Lightning NO_x emissions are distributed vertically between cloud base and cloud as discussed in (*Pickering et al*., 1998). Radon emissions are specified following the approach of *Jacob et al.* (1997).

Another important source of aerosols and trace gases in the springtime in Asia is biomass burning. In CFORS separate tracers for CO, black carbon and organic carbon from biomass burning sources are treated. Emission rates from biomass burning are highly uncertain and can change day by day. CFORS uses daily averaged CO, BC and OC emission estimates analyzed from daily AVHRR fire counts as discussed by Streets and Woo (2001) and Woo et al., (this issue).

Sea salt can play an important role in radiative transfer. Sea salt emissions and transport processes are treated using two size modes within the CFORS framework. Sea salt emissions are calculated on-line based on the work of *Gong et al*. (1997).

Volcanoes are one of the major sources of sulfur dioxide in Asia. Estimated volcano SO_2 emission for the major active volcanoes within the modeling domain are included in the analysis.

During TRACE-P large quantities of SO_2 were emitted (perhaps as much as 10 million ton-SO_2/year) from the Miyakejima Island (Mt. Oyama) just south of Tokyo.

A summary of the combustion (fossil, biofuel and in-field biomass) emissions used in the calculations is presented in **Table 1**. Further details can be found on the ACESS website http://www.cgrer.uiowa.edu/EMISSION_DATA/index_16.htm.

3. Results

Regional scale modeling that combines meteorological calculations, with on-line air mass tracers, emissions and photochemistry provides a powerful analysis framework. The mesoscale meteorological model provides a means to produce dynamic fields with higher space and time resolution than available from global archived products. Furthermore, having in a single data set information on clouds, winds, boundary-layer turbulence measures, information on aerosol and trace gas distributions, and regional emissions, facilitates forecast/planning activities and provides a valuable context for the interpretation of the observations. Snap-shots of CFORS forecasts for pollution outflow associated with frontal events during March 3 through 10, 2001 are shown in **Figure 10**. Details are discussed in **Section 3.**

3.1 Mission-wide Perspectives

The TRACE-P data set provides an excellent opportunity to test the capabilities of CTMs to represent important observed features of trace gas distributions in the western Pacific. Comparing calculated values with observed quantities provides a test of the emissions estimates, and the transport and chemical processes represented in the model. To characterize the models abilities and limitations, the model results are compared with the aircraft data. For these comparisons the 5-minute merged data sets for the P-3B and DC-8 were used. The model was sampled every five minutes along each flight-track for the period when the aircrafts were operating in the western Pacific (March 4 to April 2, 2001). Model results were interpolated to the aircraft location and time (using tri-linear interpolation). Here we focus on the post-analysis results. The evaluation of the forecast results will be the subject of a future paper.

A qualitative comparison of the calculated meteorological fields is shown in **Figure 2**. Shown are the vertical distribution of wind speed and relative humidity for all flights (DC-8 and P-3 combined). The model is able to produce the major features of the observed fields of wind speed, temperature, and pressure (not shown). Wind direction is more difficult especially in calm conditions (not shown). Relative humidity shows a high model bias at low relative humidity near the surface and at altitudes above 3 km.

Modeled and observed ethyne and ethane as a function of latitude are shown in **Figure 3**. Both species show a very strong latitudinal gradient with values increasing above 20N, consistent with the estimated emissions associated with anthropogenic activities in China, Korea and Japan. The model shows a tendency to under predict very high values, and this will be discussed in more detail later.

The comparisons discussed above are qualitative. A more quantitative analysis is obtained by examining the scatter-plots of modeled versus observed quantities. Sample results for all flights are presented in **Figure 4**. From these comparisons we see that there is a tendency for the model to under predict CO at high-observed CO values. These points are marked in red, and these same under predicted CO points are shown in the other frames as well. At the same points where we underestimate CO we tend to underestimate extinction and ethyne, but predict OH and ozone with no apparent biases. These relationships hold important information regarding emission estimates and processes and will be discussed later.

Further insights are found by looking at the relationships flight-by-flight and as a function of altitude (**Figure 5)**. Here we show that 80% of the model calculated ethane values fall within +/- 30% of the observed values, and 86% of the data is captured to within a factor of 2. Furthermore below 6 km there does not appear to be a clear bias, and the model performance seems to be more related to variations between specific outflow conditions. Above 6 km there is not a consistent bias when taken over all flights, but for some individual flights there are low or high biases that persist throughout the flight.

A summary of the performance of the model for each of the model-calculated parameters is presented in **Tables 2 and 3, and Figure 6,** for the DC-8 and P-3B platforms, respectively. For the DC-8 data, the mean values calculated by the model are within +/- 30% of the observed values for all the parameters for measurements below 1 km. Above 1 km, all the modeled mean values are within +/- 30% with the exception of RNO_3, NO_2, C_2H_6 and SO_2 in the 1-3 km region, and SO_2, NO_2 and NO for altitudes above 3 km. Below 1 km, correlation coefficients (R) are greater than ~0.7 for 21 of 31 parameters, and exceed 0.5 for all parameters except NO_2 and NO. In general the regression coefficients decrease with increasing altitude (e.g., ethane value is 0.83 at altitudes below 1 km and 0.72 at altitudes above 3 km). But a few species have their lowest R-values below 1 km (i.e., OH and HO_2). For points above 1 km, some parameters are better predicted in the 1-3 km range than above (as is the case for ozone), while others have their lowest R-values in the 1-3 km range (e.g., CO, SO_2, NO).

Further insights into the model performance as a function of height can be seen in comparing vertical profiles. The calculated and observed vertical profiles for OH, CO, C_2H_6 and C_2H_2 for the DC-8 values are presented in **Figure 7**. OH is determined largely by local conditions of water vapor, photolysis rates, and ambient levels of ozone, NO_x, CH_4 and NMHC. Analysis using Pearson correlations (linear regression analysis) indicates that the model predictions show a significant linear effect (significant linear correlation) for all vertical layers except 11 and 12. A similar story emerges for CO, C_2H_6 and C_2H_2. Due to long lifetimes of these species, their vertical distribution is determined more by emissions and transport processes. These species show enhanced values in the boundary layer, at 3-5 km, and at 6-9 km. The features at 3-5 km are associated with outflow in the warm conveyor belt region, while feature at 6-9 km is associated either with deep convection within East Asia, or long range transport from extra-Asia regions. The model profiles tend to be smoother than that observed, and are low at low altitudes, high at mid altitudes and low at high altitudes. This suggests that the cloud transport processes in the model may be too diffusive. The large variation in the lowest 1km reflects the large contrast between the clean marine air and the strong plume-like features observed in post-frontal outflow in the Yellow Sea.

To illustrate some of the sources of uncertainty in the calculations, we performed additional simulations without biomass emissions (*Tang et al., this issue, b*), without biogenic emissions, and without the effects of aerosol optical depths on photolysis calculations. Each of these represents highly uncertain quantities, and is shown to have important effects on predicted OH. The largest impacts were found for the no-aerosol case. Turning off the effect of aerosols on photolysis rates resulted in a ~40% increase in OH, and an over prediction of OH on average by ~30%. In Asia, aerosols are co-emitted with photochemical oxidant precursors and their influence on the photochemical oxidant cycle is accumulated over several days during the outflow processes as discussed in *Tang et al., (this issue, a)*. Elimination of the biogenic and biomass emissions also resulted in increases in OH values by 20% and 10%, respectively. These results underscore the need to better qualify emissions from all sources.

The model predictions of j-values, extinction and aerosol black carbon is also presented in **Table 2**. The j-values are calculated based on modeled cloud and aerosol quantities, and are predicted with similar skill as CO and ozone, and are discussed in detail in *Tang et al., (this issue, a).* The model under predicts BC by 0.1-0.2 $\mu g/m^3$, while over-predicting extinction. The BC observations are based on an optical measurement. Thus both the measured BC and modeled extinction depend heavily on the assumed optical properties, which have significant uncertainties.

Qualitatively, a similar story emerges from the comparisons with the P-3B data, although the details are different. For those parameters measured by the same groups and techniques on the 2 platforms (e.g., CO, O_3, ethane, propane, RNO_3, J-values) the model performance for the P-3B data is very similar to that for the DC-8, although the correlations vary slightly. Furthermore the mean values derived from the observations vary somewhat, reflecting differences in the sampling strategies (e.g., the P-3B flew lower, and spent more time in the boundary layer). For example in the case of CO the mean values in the 1, 1-3, and >3 km regions are for the DC-8 (and P-3B): 218.8(235.3); 188.3(208.1); and 122.4(136.1), respectively. The modeled values show a similar behavior with higher CO levels calculated for the P-3B.

For the same parameters but measured with different techniques (e.g., SO_2, sulfate, OH, HO_2, NO, and NO_2) the differences can be large. For example in the case of OH, the mean of the observed values below 1 km was 0.213 ppt on the P-3B and 0.106 ppt on the DC-8. The modeled values were also higher for the P-3B than for the DC-8, but differences were much smaller (the modeled values were 0.114 ppt for the P-3B and 0.097 ppt for the DC-8). There were also examples of the same parameter measured on the same platform using different techniques (e.g., acetone and acetaldehyde on the DC-8). Differences between the 2 measurements were observed, and the differences were present at each altitude bin. It is interesting to note that in the case of acetaldehyde, the model results are negatively correlated with one the sets of measurements, even-though the calculated mean values are quite close to the observations.

Some important discrepancies between the model and the observations are apparent. One is related to the calculated sulfur levels. The model tends to over predict SO_2 and sulfate levels in the 1-3 km range for both aircraft. This may be due to an overestimation of the emissions from the Miyakajima volcano, or to unresolved interactions with clouds. The model over predicts NO_x in the lowest layers and under predicts NO_x levels away from the surface. Due to its short-lifetime, NO_x is very sensitive to local emissions and the detailed spatial distribution, which may not be accurately reflected with an 80km horizontal resolution. The HNO_3 overestimation at low altitudes indicates that we may have underestimated the nitrate heterogeneous removal associated with aerosol-rich air masses, which may also account for the overestimation in NO_y. This will be a subject of a future paper. For the main photochemical products, O_3, PAN and RNO_3, the correlation coefficients are higher than 0.75.

The results in **Tables 2 and 3 and Figure 6** provide important insight into our present capabilities to model tropospheric trace species. The meteorological parameters are modeled most accurately, reflecting the large amount of observational data ingested into the reanalysis of the large-scale meteorological fields. The model has less skill in calculating the chemical and aerosol species. For example, in the boundary layer for the DC-8, the predictability (in terms of explaining the variance) for ethane > propane > ozone > PAN > carbon monoxide > ethene > ethyne > BC > OH > NO. These results reflect the complex interactions and interdependencies

between emissions and chemical and transport processes, and point out the challenges we face in improving our modeling capabilities.

The observations can be used to derive mission-averaged distributions. This can be done by binning the observed data to a spatial (horizontal and vertical) grid and averaging all the observed values that fall within the individual bins. Mission-averaged observed fields of ethane and carbon monoxide averaged over the lowest 2 km, and over the entire troposphere are shown in **Figures 8 and 9**. Modeled derived fields sampled and averaged the same way as the observations are also shown. Comparisons of the observed and modeled fields provide a qualitative comparison of the model predictions; the fields are qualitatively similar. What the model can provide, which the aircraft can not, is an estimate of what the mean distributions would be (in the model world) if every grid cell was sampled equally and at all times (8 to 17:00 local time) throughout the period of the TRACE-P operation. Put another way, the field experiments deploy limited resources with a prioritized list of objectives. As a result the western Pacific is not sampled randomly, but is biased towards the mission objectives (e.g., frontal outflow in biomass plume regions and downwind of megacities, etc.). Clear differences in the ethane and CO distributions measured and those calculated for the monthly averages in the Yellow Sea. This reflects the fact that the aircraft missions often sampled post-frontal outflow in this region. These events have the highest concentrations, but occur with synoptic frequency. Further details regarding frontal events is presented in the next section.

The relationships between species also can provide additional insights, as shown in **Figure 10**. Both the model and observations show two different relationships between HNO_3 and SO_2. The relationship of low nitric acid and high SO_2 are identified using back-trajectory analysis as periods where air masses impacted by volcanic emissions were encountered**.** Most of these data points are associated with P-3B flight #17 on March 26, 2001, and DC-8 flight #17 on March 31, 2001.

3.2 Case Studies

Analyses of individual flights provide insights into the model's ability to capture variations in space and time in sub-regions of the troposphere, and provide improved understanding of the strengths and weaknesses of the model. Furthermore, sensitivity studies isolating various processes or emission-categories can help evaluate sources of uncertainty, and help to quantify underlying and determining factors effecting trace gas distributions. To illustrate some of these points we present a few case studies.

3.2.1 Frontal outflow:

Characterizing the role of biomass burning and the role of frontal processes in determining the composition, location and fluxes of trace gases and aerosols in the Asian outflow were important objectives of TRACE-P. During March 7-10, the DC-8 and P-3B sampled pollution outflow as a cold front swept over East Asia. The general situation of pollution transport associated with a frontal passage is shown in **Figure 11**. The clean air in the prefrontal region, the zonal transport of pollutants off the continent at mid-latitudes at all layers when the front is passing over east Asia, the strong warm conveyor-belt transport of pollutants at 2-5 km, and the southerly transport of pollutants at low altitudes as the front moves into the western Pacific are all clearly depicted. TRACE-P sampled this frontal event at different stages of is evolution on March 7, 9 and 10 (*Tang et al., this issue, b*).

On March 7th, the P-3B and DC-8 flew flight paths shown in **Figure 12**. The observed and modeled propane distributions along the flight path show clearly outflow within the front extending to altitudes ~ 6-8 km. The DC-8 was able to fly through the front and sample prefrontal air. The comparisons of the vertical profiles of CO in the pre- and post-frontal regions are also shown. Both the observations and the model show enhancements in CO of ~200 ppb in the post-frontal air masses. Simulations with and without biomass burning were performed to help identify the source of this elevated CO. Results shown in **Figure 13** illustrate that CO in the layers above 2.5 km was due to biomass burning in SE Asia and transported in the warm-conveyor belt associated with this cold front.

The forecasts for March 9th suggested that the location of this decaying front would be located along 20N and that air influenced by biomass emissions from Southeast Asia would be

found in the warm conveyor belt of this system in a layer between 2-4 km. Air below this layer was predicted to contain pollution emitted around and north of Shanghai. On this day both the DC-8 and P-3 flew missions with flight paths along 20N.

The flight path of the DC-8, along with a sampling of the observed and modeled distributions are shown in **Figure 14**. All the species showed a significant amount of vertical structure along the flight path. The DC-8 was able to fly sufficiently far to the east to penetrate into pre-frontal air (at ~ 5 GMT). Primary species such as CO, BC and ethane showed concentrations in the prefrontal region to be ~1/3 of those in the postfrontal air. In the postfrontal region, CO and BC showed peak concentrations at 2-4 km, but with elevated levels extending to the surface. In contrast, ethane and NO_2 showed enhanced levels from the surface to ~4 km, but with peak values in the boundary layer. The model results clearly captured these features. In fact the model did an excellent job in quantitatively capturing many of these import features, including the location and magnitude of the peaks, the post-frontal enhancements, and the vertical variability.

Calculated OH values are also shown. In many sections of the flight, modeled OH closely tracked the observed values. However, in the period of 2.5 to 5 GMT, OH in the model decreased in the boundary layer, as did the observations, but the model values went significantly lower. As the DC-8 climbed out of the boundary, both the observed and modeled values increased. As the aircraft climbed above 5 km, observed OH continued to increase, while the modeled values decreased. To help understand this behavior the observed and modeled J [O^1D] values are also presented. The predicted values are too low in the boundary layer around 2.5 GMT, due to an overestimation of the attenuation by the calculated aerosol and cloud distributions. However, the calculated J-values during the assent and at the high altitude leg are accurately captured, as are the acetone, formaldehyde, ethane and CO values. The reasons for the discrepancies remain an open question.

The forecasted biomass-burning tracer (CO) along 20N is presented in **Figure 15**. Also shown are the observed CO distribution and the observed soluble aerosol K^+ concentrations (potassium is a good tracer of biomass burning) measured on the P-3. The observed layer of enhanced K^+ is found in the warm sector outflow at the latitude and altitudes forecasted. Three-

dimensional back trajectories for each 5-minute flight segment for all flights were calculated from our 3- dimensional wind fields. Trajectories for the flight segment 2:30 to 3:30 GMT, color coded with calculated CO levels along the trajectory, are also shown in **Figure 15**. These results indicate that the air sampled above ~2 km was influenced by biomass burning emissions approximately 4 days previously, and that this air was lifted by orographic forcing over the highlands of northern Southeast Asia to nearly 4 km, and then descended to 2-3 km in the leading edge of the surface high pressure system centered of Vietnam (see **Figure 11**). In contrast air below 2 km passed at low altitude over the source regions of eastern China and traveled south in the low-level winter monsoon flow.

To further illustrate the complex nature of outflow during frontal passages in East Asia, we calculated three-dimensional forward trajectories from different source regions. Trajectories were initiated every 3 hours over a biomass-burning region in SE Asia, and over major emitting cities of Chongqing, Shanghai and Qingdao over the period March 3-10. Each trajectory was followed for 5 days. The results are shown in **Figures 16 and 17**. For biomass burning emissions over Myanmar, we see that during this period all the forward trajectories initiated at 1 km over the source region lead to outflow into the western Pacific at altitudes between 3-6 km. The air masses are lifted by orographic effects associated with the mountains in northern Laos, Vietnam and southern China, and aided by convection.

Chongqing is a heavily polluted region located in a basin just east of the Tibet plateau. Outflow from this region is complex, and restricted to easterly outflows as transport to the west is blocked. The transport out of this region is very intermittent, with trajectories remaining over Central China for periods of days between frontal events, and being transported to latitudes below 30N during post-frontal periods. Emissions from the coastal cities of Shanghai and Qingdao experience northerly, easterly and ascending transport with the approach of the low-pressure system, and southerly low altitude transport associated with trailing high-pressure systems. In these winter monsoon flows, we see that the latitudinal gradient in emissions is transformed into a longitudinal gradient at lower latitudes. For example the flights at low altitude on March 9th at 20N were sampling air of different age and from different source regions. Air from Shanghai was expected to be found at lower longitudes, while emissions from Qingdao

were expected to be located farther to the east. We also see that air from northern China can affect pollution levels over southern China.

Calculated fluxes during the period March 1-14 are presented in **Figures 18 and 19**. The vertical distributions show clearly the major outflow regions. In the case of CO the major outflow conditions along ~125E show two distinct flux regions, one at lower latitudes associated with biomass burning, and the second at higher latitudes heavily influenced by fuel combustion sources. The major outflow occurs between 3-6 km, and rises to 3-8 km along the eastern boundary, associated with lifting within the frontal system as the air masses move into the western Pacific. Similar features are seen for HCHO, but the absolute flux decreases at the eastern boundary, reflecting the chemical destruction of HCHO. Further details are found in the horizontal flux plots (**Figure 19**). The low altitude fluxes reflect the major source areas, and the split in the transport patterns between those sources above 30N and those below. It is interesting to note the high flux region in and around Hainan, which represents a convergence zone where pollutants emitted from northern China and transported in the monsoon flow are brought together with the outflow of fresh emissions from south China.

These results help to illustrate the complex nature of pollutant transport associated with frontal events in the springtime in East Asia.

3.2.2 Yellow Sea:

Many flights operated in the Yellow Sea to look at outflow downwind of the high source regions in eastern China. One such experiment was the P-3B flight #14 conducted on March 18, 2001. On March 17 a developing wave cyclone was located east of Shanghai, and an anticyclone was centered just east of Tokyo. The wave cyclone intensified during the day and moved eastward, and its associated cold front also swept towards the east. On March 18 the wave cyclone was located just off the northeast coast of Japan; and was moving towards the northeast. Pollutants were transported off the cost of China at low altitudes and towards Japan as this front swept to the east.

The flight path of the P-3B and observed and measured values are presented in **Figure 20**. Throughout the flight path in the Yellow Sea elevated levels of pollutants were found at multiple levels between the surface and ~ 2 km. The model values show these features, and a wide variety of calculated primary and secondary species agree well with the measured values. As discussed previously, the model consistently under predicted CO at low altitudes in the Yellow Sea, and this is clearly shown in the low altitude leg at ~ 3 GMT. However, the calculated values for SO_2, ethene, and NO_2, while under predicted, are much closer to the observed values. These results suggest that there are many fine scale structures, associated with plumes that are not resolved by the model at 80 km horizontal resolution. The P-3B observed an elevated layer of ozone at 5 km on the return to Japan. This layer was not elevated in CO, suggesting either a well-aged or stratospheric source. The model captured this feature, but the peak value was dramatically under estimated.

3.2.3 Emission Estimates

Emission estimates in East Asia are uncertain, and in the case of many species, such as speciated hydrocarbons, have only recently been estimated (some prepared specifically for TRACE-P and ACE-Asia). Furthermore comprehensive measurements of atmospheric composition that can be used to evaluate emission estimates are often lacking. Measurements obtained in TRACE-P provide a means to evaluate the quality of emission estimates. Results presented so far in this paper have provided some measure of the quality of the estimated emissions. Since the model calculations are driven by the emissions, a comparison of the predictions with the observations provides a first-order estimate of the quality of the emissions. Based on the comparisons presented in previous sections we can conclude that the inventory performs well for the light alkanes, CO, ethylene, SO_2, NO_x. Furthermore, since the model shows some skill in predicting important photochemical species such as O_3, HCHO, OH, HO_2, and HNO_3, this implies that the emissions inventories are of sufficient quality to support preliminary studies of ozone production. On the other hand, the above analysis has clearly pointed out problem areas as well. For example the tendency to under predict CO and BC at low altitudes in the Yellow Sea. A comprehensive evaluation of emission estimates is the focus of *Carmichael et al.,* (this issue).

3.2.4 Ozone Production

Emissions of NO_x and NMHCs have increased significantly over the last decade in Asia, and as a result urban and regional ozone levels have increased. The TRACE-P experiment provides an opportunity to add some insights into ozone production in the region, and into how well current emission estimates and models can represent the photochemical oxidant cycle. As discussed previously the model is able to predict with some skill the major species and parameters involved in the photochemical oxidant cycle including, NO_x. NMHCs, OH, O_3, and photolysis rate, especially in the lowest few kilometers. These results provide a strong basis upon which to begin to explore ozone production and its sensitivity to NO_x and NMHC emissions in East Asia.

Insights into ozone production can be obtained by using observation-based analysis. One commonly used measure of ozone production is derived from the relationship between ambient ozone and NO_z levels. The observed relationship from the aircraft observations is shown in Figur**e 20**. The mission-wide data show different behavior at low and high NO_z levels. The low NO_z values correspond to high altitude data, while the high NO_z values are associated with low altitude data. We used the back-trajectory analysis discussed previously to classify the observations according geographical origin of the air masses; and used these points to estimate ozone production efficiency. To illustrate, the points identified as being most heavily influenced by emissions from Shanghai and central China are highlighted in **Figure 21**, and the observed ozone to NO_z slope was calculated to be 3.4. The model-based analysis is also shown and the estimated production efficiency is 3.5. The values derived from the observations as a function of region are shown in **Table 4.** The ozone production rates vary dramatically from region to region. While these rates can only be considered qualitative (and with a high level of uncertainty) at best, they do illustrate how information can be mined from the observations.

The comprehensive measurements of key photochemical species during TRACE-P provide valuable insights into what controls the production of ozone. Of fundamental importance to understanding what limits ozone production is a determination of whether the loss processes of

HO_x are controlled by NO_x or NMHC reactions. *Kleinmam (2000)* developed a procedure to estimate these processes from measured or modeled quantities. Shown in **Figure 22** is the model-derived ratio of radical loss by NO_x processes to total radical production as a function of NO_x levels for all DC-8 and P-3B data points below 3 km. In this analysis, values of LN/Q above 0.5 indicate air masses in which ozone production is hydrocarbon limited, and values less than 0.5 indicate conditions where ozone production is NO_x limited. Also shown are data points identified to have been influenced by emissions from megacities, and the age of these air masses as determined by back trajectory analysis. We see many situations where ozone production is hydrocarbon limited, and these are not solely limited to air masses that are less than 1 day old. The majority of the data points indicate NO_x limited conditions. Again these are not only restricted to aged air masses.

Finally, we further explored the relative importance of NO_x and NMHC in ozone production in East Asia, by performing model calculations for the month of March for cases where we doubled energy-related (i.e., biofuel and fossil fuel emissions) NO_x and NMHC emissions separately. The change in ozone for each of the data points along the flight paths of the DC-8 and P-3B are presented in **Figure 23**. We see again that the majority of the data points indicate NO_x–limited conditions (i.e., ozone increases when NO_x emissions increase). However we see regions where O_3 decreases with increases in NO_x, as well as cases where ozone decreases with increasing NMHC, and where increasing NMHC increases ozone. The back trajectories for the data points where ozone decreased with increasing NO_x are also presented. From this analysis we see that all data points have trajectories from Tokyo, Seoul, Shanghai and coastal areas of NE China. (In general the negative NO_x response and positive NMHC responses are corresponding points.) This is more clearly seen in the March-averaged change in near surface ozone. The area of decreases in ozone due to increases in NO_x reflects the highly industrialized regions of East Asia, where fossil fuel usage dominates. South of ~30-35N, ozone production is NO_x-limited, reflecting the high NMHC/NO_x ratios due to the large contributions to the emissions from biomass burning, biogenics sources, and biofuel usage in central China and SE Asia.

4. Summary

During the TRACE-P experiment, the CFORS/STEM-2K1, regional-scale chemical transport model, was used in forecast mode to aid in mission planning, and in hind-cast mode to help interpret the aircraft data. Results presented demonstrate that regional scale modeling that combines meteorological calculations with on-line air mass tracers, emissions and photochemistry provides a powerful analysis framework. The mesoscale meteorological model provides a means to produce dynamic fields with higher space and time resolution than available from global archived products. Furthermore, having in a single data set information on clouds, winds, boundary-layer turbulence measures, information on aerosol and trace gas distributions, and regional emissions, facilitates forecast/planning activities and provides a valuable context for the interpretation of the observations.

The regional model was shown to accurately predict many of the important features observed. For example when compared to all 5-minute averaged ethane measurements, 80% of the model calculated ethane values fell within +/- 30% of the observed values, and 86% of the data was captured to within a factor of 2. When all the modeled parameters were analyzed it was found that the meteorological parameters were modeled most accurately, reflecting the large amount of observational data ingested into the reanalysis of the large-scale meteorological fields. The model has less skill in calculating the chemical and aerosol species. For example, in the boundary layer for the DC-8, the predictability (in terms of explaining the variance) for ethane > propane > ozone > PAN > carbon monoxide > ethene > ethyne > BC > OH > NO. These results reflect the complex interactions and interdependencies between emissions and chemical and transport processes, and point out the challenges we face in improving our modeling capabilities.

Case studies of frontal outflow and transport into the Yellow Sea were presented and showed the complex nature of outflow in East Asia. Biomass burning from SE Asia was shown to be an important source of observed outflow, and to be transported in the warm conveyor belt at altitudes above ~2 km and at latitudes below 30N. Outflow of pollution emitted along the east coast of China in the post frontal regions was shown to be confined to the lower ~2 km and to result in high concentrations in the Yellow Sea. During these situations the model under predicted CO and BC (among other species). The importance of model resolution versus inaccuracies in emissions remains to be quantified.

Based on the comparisons between observed and modeled quantities we conclude that the emission inventory performs well for the light alkanes, CO, ethylene, SO_2, NO_x. Furthermore, since the model showed some skill in predicting important photochemical species such as O_3, HCHO, OH, HO_2, and HNO_3, this implies that the emissions inventories are of sufficient quality to support preliminary studies of ozone production. On the other hand, the analysis pointed out problem areas as well, most notable was the tendency to under predict CO and BC at low altitudes in the Yellow Sea.

We have shown how the results from this experiment could be used to assess ozone production in East Asia. Ozone is emerging as one of the primary air pollution issues in the region. However analysis and design of control strategies is limited by the lack of detailed emissions inventories, and measurements upon which to assess ozone production and to test air pollution models. The TRACE-P experiment has produced a data set that we can use to test our ability to model ozone formation in East Asia (in the springtime). Form this data we have estimated ozone production efficiencies, and found them to be highest in SE Asia outflow and minimum in the Yellow Sea. We estimated the relative importance of NO_x and NMHC in ozone production in East Asia. Throughout most of the region during the period of the experiment ozone production was NO_x-limited. NMHC limited conditions were identified in the highly industrialized regions of East Asia, where fossil fuel usage dominates. South of ~30-35N, ozone production was found to be NO_x-limited, reflecting the high NMHC/NO_x ratios due to the large contributions to the emissions from biomass burning, biogenics sources, and biofuel usage in central China and SE Asia.

Acknowledgements

This work was supported in part by grants from the NASA GTE and ACMAP programs and the NSF Atmospheric Chemistry Program. This work (I. Uno) was also partly supported by Research and Development Applying Advanced Computational Science and Technology (ACT-JST) and the CREST of Japan Science and Technology Corporation.

References:

Carter, W., Documentation of the SAPRC-99 chemical mechanism for voc reactivity assessment, Final Report to California Air Resources Board Contract No. 92-329, University of California-Riverside, May 8, 2000.

Gillette, D., and R. Passi, Modeling Dust Emission Caused by Wind Erosion, *J. Geophys. Res.,* 93, 14233-14242, 1988.

Gong, S. L., L. A. Barrie, and J.-P. Blacnchet, Modeling sea-salt aerosols in the atmosphere 1. Model development, *J. Geophys. Res.*, 102, 3805-3818, 1997.

Jacob, D. J. *et al*., Evaluation and intercomparison of global atmospheric transport models using radon-222 and other short-lived tracers, *J. Geophys. Res.*, 102, 5953-5970, 1997.

Kleinman ,L. L, Ozone process insights from field experiments – part II: Observation-based analysis for ozone production, *Atmos.Environ*. , 34, 2023-2033, 2000.

Madronich, S., and S. Flocke, The role of solar radiation in atmospheric chemistry, in Handbook of Environmental Chemistry (P. Boule, ed.), Springer-Verlag, Heidelberg, 1-26, 1999.

Pickering, K. E., Y. Wang, W.-K. Tao, C. Price, and , J. –F. Muller,Vertical distributions of lightning NOx for use in regional and global transport models, *J. Geophys. Res.*, 10**3**, 31203-31216, 1998.

Pielke, R. A., W. R. Cotton, R. L. Walko, C. J. Tremback, W. A. Lyons, L. D. Grasso, M. E. Nicholls, M. D. .Moran, D. A. Wesley, T. J. Lee , and J. H. Copeland, A comprehensive meteorological modeling system -RAMS, *Meteorol. Atmos. Phys.*, 49, 69-91, 1992.

Phadnis, M. J. Tropospheric Air Pollution Modeling on a Regional Scale: Case Studies for East Asia and South East Asia. Ph.D. Thesis, Department of Chemical and Biochemical Engineering, University of Iowa, Iowa City, 1999.

Phadnis, M. J. and G. R. Carmichael, Influence of mineral aerosol on the tropospheric chemistry of East Asia, *J. Atmos. Chem,* 36, 285-323, 2000.

Phadnis, M. J. and G. R. Carmichael, Forest Fire in the Boreal Region of China and its Impact on the Photochemical Oxidant cycle of East Asia, *Atmos. Environ.*, 34(3), 483-498, 2000a.

Street, D. G., T. C. Bond, G. R. Carmichael, S. D. Fernandes, Q. Fu, D. He, Z. Klimont, S. M. Nelson, N. Y. Tsai, M. Q. Wang, J.-H. Woo, and K. F. Yarber, An inventory of gaseous and primary aerosol emissions in Asia in the year 2000, *J. Geophys. Res* . (this issue).

Streets, D. G. and J.-H. Woo, http://www.cgrer.uiowa.edu/ACESS/EMISSION_DATA/ED_index.htm. and http:// www.cgrer.uiowa.edu/people/woojh21/data_fire_co_index.html.

Song, C. H., Tropospheric Aerosol in East Asia: A Model Study of the Evolution Processes of Dust and Sea Salt Particles During Long Range Transport, PhD Thesis, Department of Chemical & Biochemical Engineering, University of Iowa, 1999.

Song, C. H., and G. R. Carmichael, The Aging Processes of Naturally Emitted Aerosol During Long Range Transport, *Atmos. Environ.*, 33, 2203-2218, 1999a.

Song, C. H., and G. R. Carmichael, A Three-dimensional modeling investigation of the evolution processes of dust and Sea Salt particles in east Asia, *J. Geophys. Res.,* 106(D16), 18131-18153, 2001.

Tang, Y., G. R. Carmichael, I. Uno, J.-H. Woo, G. Kurata, B. Lefer, R. E. Shetter, H. Huang, B. E. Anderson, M. A. Avery, A. D. Clarke and D. R. Blake, Impacts of aerosols and clouds on photolysis frequencies and photochemistry during TRACE-P, part II: three-dimensional study using a regional chemical transport model, *J. Geophys. Res.*, (this issue, a).

Tang, Y., G. R. Carmichael, J.-H. Woo, N. Thongboonchoo, G. Kurata, I. Uno, D. G. Streets, D. R. Blake, R. J. Weber, R. W. Talbot, Y. Kondo and H. B. Singh, The Influences of Biomass Burning during TRACE-P Experiment Identified by the Regional Chemical Transport Model, *J. Geophys. Res.* (this issue, b).

Underwood, G. .M., C. H. Song, M. Phadnis, G. R. Carmichael, and V. H. Grassian, Heterogeneous Reactions of NO_2 and HNO_3 on oxides and mineral dust: A Combined Laboratory and Modeling Study, *J. Geophys. Res.,* 106(D16), 18055-18066, 2001.

Uno, I., H. Amano, S. Emori, K. Kinoshita, I. Matsui, and N. Sugimoto, Trans-Pacific yellow sand transport observed in April 1998: A numerical simulation, *J. Geophys. Res.*, 106(D16), 18331-18344, 2001.

Uno, I., G. R. Carmichael, D. G. Streets, Y. Tang, J. J. Yienger, S. Satake, Z. Wang, J.-H. Woo, S. Guttikunda, M. Uematsu, K. Matsumoto, H. Tanimoto, K. Yoshioka, and T. Iida, Regional Chemical Weather Forecasting using CFORS; Analysis of Surface Observation at Japanese Island Station during the ACE-Asia Experiment, submitted *J. Geophys. Res.,* 2002.

Verwer, J. G., E. J. Spee, J. G. Blom, and W. H. Hundsdorfer, A second order Rosenbrock method applied to photochemical dispersion problems. Modelling, Analysis and Simulation (MAS), MAS-R9717, August 31, 1997.

Woo, J.-H., D. G. Streets, G. R. Carmichael, Y. Tang, B.-I. Yoo, W.-C. Lee, N. Thongboonchoo, S. Pinnock, G. Kurata, and I. Uno, Biomass and Biofuel Emissions and Their Impact on Trace Gas Distributions in Asia during the TRACE-P Experiment. **,** *J. Geophys. Res.*(this issue).

Xiao, H., G. R. Carmichael, J. Durchenwald, D. Thornton, and A. Bandy ,Long-range transport of SOx and dust in East Asia during the PEM B Experiment, *J. Geophys. Res.*, 102, 28,598-28,612, 1997.

Zhang, Y., and G. R. Carmichael, Interactions of mineral aerosol with tropospheric chemistry, *J Appli. Meteor.,* 38: 353, 366, 1999.

Figure Captions:

Figure 1. Schematic diagram of the CFORS/STEM-2K1 regional-scale modeling system used in support of the TRACE-P experiment.

Figure 2. Measured and modeled wind speed and water vapor mixing ratios for the DC8 and P3 aircraft data. Shown are values for each 5-minute flight segments from the merged data set.

Figure 3. Measured and modeled ethyne and ethane mixing ratios for the DC8 and P3 aircraft data. Shown are values for each 5-minute flight segments from the merged data set.

Figure 4. Comparison of measured and modeled trace gas and extinction for the DC8 and P3 aircraft data. Shown are values for each 5-minute flight segments from the merged data set. Red points indicate points where the model underestimates CO.

Figure 5. Comparison of observed and modeled ethane mixing ratios for the DC8 and P3 aircraft data. Shown are values for each 5-minute flight segments from the merged data set. Black designates points where modeled values are within +/- 30% of observed. Changing colors designate additional levels of +/- 30%.

Figure 6. Correlation coefficients for the data presented in Tables 2 and 3.

Figure 7. Comparison of the observed and modeled vertical profiles of OH, C_2H_6, CO, and C_2H_2 for the DC8 data. Shown are values for each 5-minute flight segments from the merged data set.

Figure 8. Mission-perspective ethane distributions. Averaged observed distribution using all P3 and DC8 5-minute merged data (a). Same as above but based on predicted values sampled and averaged for the same flight segments (c). Averaged observed distribution using the P3 and DC8 5-minute merged data for the altitude-range 0-2km (b). Model calculated mean values using all modeled values between 8:00 to 18:00, and 0-2 km, for the month of March (d).

Figure 9. Mission-perspective CO distributions. Averaged observed distribution using all P3 and DC8 5-minute merged data (a). Same as above but based on predicted values sampled and averaged for the same flight segments (c). Averaged observed distribution using the P3 and DC8 5-minute merged data for the altitude-range 0- 2km (b). Model calculated mean values using all modeled values between 8:00 to 18:00, and 0-2 km, for the month of March (d).

Figure 10. Observed and modeled relationships between SO_2 and HNO_3 for the DC8 and P3 aircraft data. The high SO_2 and low HNO_3 data represent aircraft observations influenced by the Miyakajima volcano.

Figure 11. Forecasts of pollution outflow during the frontal events of March 2 (top left) through March 10 (lower right). Shown are clouds (white), BC iso-surface (>1ug/m3) colored by % due to biomass burning (red > 50%), 3 km streamlines (orange), wind vectors at 600 m (blue) at 6 GMT.

Figure 12. Observed and simulated vertical profiles of CO on DC8 flight #7 in the pre and post front regions. Also shown are the observed and calculated propane mixing ratios for the DC8 flight #7 and P3 flight #9.

Figure 13. Calculated contribution of CO (percentage) due to biomass burning obtained by runs with the biomass burning sources.

Figure 14. Comparison of observed and predicted species along the DC8 flight #7 path on March 9 using the 5-minute merged data set.

Figure 15. Forecast of CO due to biomass burning along 20N at 3 GMT (12 Japan Standard Time – JST) on March 9 (top). Observed CO and aerosol potassium are also shown. Potassium provides a good tracer for biomass burning.

Figure 16. 5-day back trajectories every five minutes along the DC8 flight path from 2:30 – 3:30 GMT for flight #8. Trajectories are colored by modeled CO.

Figure 17. 5-day forward trajectories from a biomass source region in SE Asia (a), Chongqing (b), Shanghai (c), and Qingdao (d).

Figure 18. Calculated vertical profiles of horizontal fluxes for HCHO and CO along the surfaces indicated averaged over March 1 – 14.

Figure 19. Calculated horizontal fluxes of CO and HCHO for different vertical layers, averaged over March 1-14. Vector indicates the flux direction. Both color and length of vector represent magnitude.

Figure 20. Comparison of observed and predicted species along the P3 flight path on March 18 using the 5-minute merged data set.

Figure 21. Observed relationship between O_3 and NO_z based on DC8 and P3 data (5-minute merged colored in altitude of the observation (a); ozone production efficiencies for points identified by back trajectory analysis to have passed over Central China at altitudes below 2 km (b). Both observed and model-based analysis is shown.

Figure 22. Calculated ratio of radical loss due to nitrogen-oxide related processes to total radical loss, for each 5-minute segment of the DC8 and P3 data. Also shown is the estimated age of the air mass from passing over a major city within 2 km as determined by the back trajectory analysis.

Figure 23. Response of calculated ozone at the locations of the aircraft observations due calculated for simulations where anthropogenic NO_x and NMHC are increased by 2 times (separately).

Table 1. Emissions used in this study.

	China			Japan			Korea(ROK)			Korea(DPRK)			Mongolia			Taiwan, ROC		
	Ant.	BB	Total	Ant.	BB	Total	Ant.	BB	Total	Ant.	BB	Total	Ant.	BB	Total	Ant.	BB	Total
SO_2	1724.3	12.1	1736.4	67.9	0.2	68.2	70.3	0.1	70.4	19.2	0.2	19.4	7.1	0.2	7.3	31.9	0.1	32.0
NO_x	894.4	105.8	1000.2	185.9	1.8	187.7	111.7	0.8	112.5	22.5	1.0	23.6	3.2	2.3	5.6	44.1	0.4	44.5
CO	8493.6	2463.0	10956.6	558.5	43.4	601.9	225.6	20.2	245.7	286.4	24.1	310.5	29.8	32.2	62.0	176.2	11.4	187.6
CH_4	3129.1	85.9	3215.0	87.6	1.4	89.0	93.4	0.6	94.0	108.1	0.9	109.0	31.8	1.2	33.1	49.0	0.4	49.5
NH_3	1133.3	34.5	1167.8	29.6	0.6	30.2	14.4	0.3	14.7	8.1	0.3	8.4	9.9	0.5	10.4	12.9	0.2	13.0
CO_2	300.1	41.2	341.3	101.9	0.7	102.6	34.7	0.3	35.0	10.0	0.4	10.4	1.4	0.7	2.1	16.9	0.2	17.1
BC	79.5	17.7	97.2	4.4	0.3	4.7	1.8	0.1	1.9	1.8	0.1	2.0	0.2	0.2	0.4	0.7	0.1	0.7
OC	225.7	104.0	329.7	5.3	2.1	7.4	1.8	0.8	2.6	8.0	1.5	9.6	0.8	2.1	2.9	0.6	0.5	1.1
PM_{10}	933.2	339.0	1272.2	23.3	6.4	29.7	11.5	2.9	14.4	28.5	3.7	32.2	6.0	4.6	10.5	5.1	1.5	6.6
$PM_{2.5}$	508.6	137.9	646.5	13.5	2.7	16.3	5.5	0.9	6.4	15.7	2.1	17.8	3.1	3.2	6.3	2.1	0.6	2.7
Ethane	69.4	26.7	96.1	2.3	0.4	2.7	2.0	0.2	2.2	0.6	0.2	0.8	0.1	0.2	0.2	0.8	0.1	0.9
Propane	51.5	12.5	64.0	3.1	0.2	3.3	2.9	0.1	3.0	0.5	0.1	0.6	0.1	0.1	0.1	1.3	0.1	1.3
Butane	75.3	2.0	77.3	14.5	0.0	14.5	11.8	0.0	11.8	1.7	0.0	1.7	0.2	0.0	0.2	7.0	0.0	7.0
Pentane	56.4	0.7	57.1	6.2	0.0	6.2	5.4	0.0	5.4	1.3	0.0	1.3	0.2	0.0	0.2	2.5	0.0	2.5
Oth.Alkane	154.2	6.4	160.7	25.4	0.1	25.6	20.7	0.1	20.7	3.0	0.1	3.1	0.4	0.1	0.4	10.2	0.0	10.2
Ethene	130.2	40.6	170.8	4.8	0.7	5.4	4.6	0.3	4.9	0.8	0.3	1.1	0.1	0.4	0.5	1.2	0.2	1.4
Propene	48.3	25.3	73.6	2.3	0.4	2.8	2.5	0.2	2.7	0.3	0.2	0.5	0.0	0.2	0.2	0.7	0.1	0.8
T. Alkene	34.8	12.8	47.7	2.0	0.2	2.2	1.6	0.1	1.7	0.4	0.2	0.5	0.0	0.2	0.2	0.6	0.1	0.6
I. Alkene	53.2	3.5	56.7	2.2	0.1	2.3	1.9	0.0	1.9	0.4	0.0	0.5	0.1	0.0	0.1	0.7	0.0	0.7
Acetylene	70.2	10.3	80.5	1.6	0.2	1.8	2.1	0.1	2.2	0.5	0.1	0.6	0.0	0.1	0.2	0.5	0.0	0.6
Benzene	53.8	5.7	59.5	1.3	0.1	1.4	1.1	0.0	1.2	0.5	0.1	0.5	0.0	0.1	0.2	0.4	0.0	0.4
Toluene	115.6	2.7	118.3	13.1	0.1	13.1	8.5	0.0	8.5	2.0	0.1	2.1	0.2	0.1	0.3	4.2	0.0	4.2
Xylene	44.3	0.9	45.2	5.2	0.0	5.2	2.8	0.0	2.8	0.9	0.0	0.9	0.1	0.0	0.1	1.2	0.0	1.2
Oth. Aromatics	86.8	2.6	89.4	7.7	0.1	7.8	5.8	0.0	5.8	1.4	0.0	1.4	0.2	0.0	0.2	2.2	0.0	2.3
HCHO	14.3	39.6	53.9	2.0	0.8	2.8	1.4	0.3	1.8	0.2	0.5	0.7	0.0	0.4	0.4	0.7	0.2	0.8
Oth. Aldehydes	20.6	27.8	48.3	0.5	0.5	1.0	0.5	0.2	0.7	0.0	0.3	0.3	0.0	0.4	0.4	0.1	0.1	0.3
Ketones	12.8	56.5	69.4	3.5	1.0	4.5	1.5	0.5	1.9	0.2	0.5	0.7	0.0	0.6	0.7	0.8	0.3	1.0
Halocarbones	16.4	5.7	22.1	5.8	0.1	5.9	2.1	0.1	2.2	0.2	0.0	0.3	0.0	0.0	0.0	1.0	0.0	1.1
Others	160.6	145.3	305.9	58.2	2.8	61.0	18.5	1.1	19.6	2.2	1.9	4.2	0.3	2.5	2.8	7.2	0.7	7.9

Table 1. continue (Southeast Asia)

	Brunei			Cambodia			Indonesia			Laos			Malaysia			Myanmar			Philippines			Singapore			Thailand			Vietnam		
	Ant.	BB	Total	Ant.	BB	Total	Ant.	BB	Total	Ant.	BB	Total	Ant.	BB	Total	Ant.	BB	Total	Ant.	BB	Total	Ant.	BB	Total	Ant.	BB	Total	Ant.	BB	Total
SO_2	0.5	0.0	0.5	2.9	2.6	5.5	71.0	7.1	78.1	0.7	6.9	7.6	22.1	3.1	25.2	2.6	15.8	18.4	59.5	3.6	63.1	13.9	0.0	13.9	79.2	11.4	90.6	15.1	7.2	22.3
NO_x	1.7	0.0	1.7	2.3	26.6	28.9	85.3	45.9	131.2	1.5	42.1	43.6	37.1	13.6	50.7	5.4	75.6	81.0	21.8	20.2	42.1	15.7	0.0	15.7	76.2	77.5	153.7	12.7	62.7	75.4
CO	1.3	0.0	1.3	48.4	486.0	534.4	1201.2	1313.4	2514.7	16.5	1270.5	1287.0	270.3	564.7	835.0	185.1	2910.8	3095.8	144.6	702.1	846.7	11.7	0.0	11.7	474.5	2140.6	2615.1	537.8	1372.1	1909.9
CH_4	4.2	0.0	4.2	63.3	24.2	87.5	526.0	77.1	603.2	21.5	77.0	98.6	59.6	36.3	95.9	225.9	182.4	408.3	156.9	38.9	195.8	10.4	0.0	10.4	321.4	120.0	441.4	267.2	69.0	336.2
NH_3	0.2	0.0	0.2	5.9	6.9	12.8	108.1	17.3	125.3	2.3	16.5	18.9	9.8	7.1	16.9	22.2	36.9	59.1	20.6	9.1	29.7	0.4	0.0	0.4	27.0	28.4	55.4	54.8	19.0	73.8
CO_2	0.9	0.0	0.9	1.2	9.5	10.6	37.2	22.0	59.1	0.4	21.0	21.4	9.2	8.6	17.8	4.1	45.0	49.1	9.8	10.9	20.7	4.8	0.0	4.8	22.3	36.0	58.3	9.9	24.8	34.7
BC	0.0	0.0	0.0	0.6	3.3	3.9	12.5	8.6	21.2	0.2	8.3	8.5	1.0	3.6	4.6	2.1	18.7	20.8	1.7	4.7	6.4	0.3	0.0	0.3	3.1	14.2	17.4	5.8	9.4	15.2
OC	0.0	0.0	0.0	2.7	24.3	27.0	59.0	65.0	124.0	0.9	63.6	64.5	2.8	28.0	30.8	9.6	143.3	152.8	6.9	32.4	39.3	0.2	0.0	0.2	9.4	103.7	113.1	24.8	65.7	90.6
PM_{10}	0.3	0.0	0.3	9.3	56.1	65.4	171.0	141.1	312.0	3.0	133.9	136.8	18.1	57.7	75.8	29.5	302.3	331.8	21.9	78.7	100.6	6.1	0.0	6.1	31.1	236.3	267.4	75.7	159.2	234.9
$PM_{2.5}$	0.2	0.0	0.2	5.8	40.0	45.9	106.6	110.5	217.1	1.9	109.3	111.2	9.4	48.6	58.0	18.8	246.8	265.5	13.4	52.7	66.2	3.7	0.0	3.7	18.9	172.9	191.8	47.3	106.5	153.8
Ethane	0.6	0.0	0.6	0.6	4.6	5.1	31.7	15.2	46.9	0.2	14.9	15.2	4.8	7.2	12.0	2.4	36.6	39.0	3.9	8.7	12.6	0.1	0.0	0.1	7.4	24.6	32.0	5.4	14.4	19.8
Propane	0.5	0.0	0.5	0.1	0.9	1.1	13.7	2.4	16.1	0.1	2.1	2.2	3.8	1.0	4.8	0.8	5.4	6.2	2.8	2.0	4.8	0.2	0.0	0.2	4.6	4.7	9.3	1.8	3.4	5.2
Butane	0.4	0.0	0.4	0.5	0.3	0.8	15.5	0.8	16.3	0.3	0.7	1.1	6.1	0.3	6.5	1.9	1.8	3.7	3.0	0.5	3.5	0.5	0.0	0.5	10.0	1.3	11.3	2.8	0.8	3.7
Pentane	0.2	0.0	0.2	0.4	0.1	0.5	10.6	0.2	10.8	0.3	0.2	0.5	4.5	0.1	4.6	1.6	0.5	2.0	1.9	0.1	2.1	0.4	0.0	0.4	8.0	0.3	8.3	2.2	0.2	2.4
Oth.Alkane	1.5	0.0	1.5	1.0	1.2	2.2	49.8	3.1	52.9	0.7	3.0	3.7	18.4	1.3	19.7	5.7	6.8	12.5	8.4	1.7	10.1	0.9	0.0	0.9	29.1	5.1	34.2	7.0	3.3	10.4
Ethene	0.0	0.0	0.0	1.3	8.4	9.7	59.1	25.8	84.9	0.6	25.4	26.0	6.1	11.9	17.9	5.6	60.4	66.0	8.4	14.0	22.4	0.4	0.0	0.4	17.5	41.4	58.9	11.8	24.8	36.6
Propene	0.0	0.0	0.0	0.5	2.7	3.2	23.4	7.8	31.3	0.2	7.3	7.5	2.4	3.4	5.8	2.1	18.0	20.0	3.4	5.3	8.7	0.1	0.0	0.1	7.1	13.8	20.9	4.4	9.0	13.4
T. Alkene	0.0	0.0	0.0	0.3	2.8	3.2	15.7	7.9	23.6	0.1	7.7	7.9	1.8	3.5	5.3	1.3	17.8	19.1	2.3	4.1	6.4	0.2	0.0	0.2	5.0	12.7	17.6	2.7	7.9	10.6
I. Alkene	0.0	0.0	0.0	0.6	0.7	1.4	24.5	2.4	26.9	0.3	2.4	2.7	3.0	1.1	4.2	2.5	5.6	8.1	3.5	1.3	4.7	0.1	0.0	0.1	8.1	3.8	11.9	5.1	2.2	7.3
Acetylene	0.0	0.0	0.0	0.6	2.2	2.7	25.4	5.7	31.1	0.2	5.5	5.7	2.4	2.4	4.8	2.3	12.4	14.7	4.1	3.0	7.1	0.1	0.0	0.1	7.2	9.3	16.5	5.1	6.0	11.1
Benzene	0.0	0.0	0.0	0.5	1.9	2.4	36.4	5.3	41.7	0.2	5.3	5.5	2.6	2.4	5.0	2.2	11.9	14.1	4.5	2.5	7.0	0.1	0.0	0.1	10.7	8.2	18.9	4.9	5.0	9.8
Toluene	0.1	0.0	0.1	0.6	1.3	1.9	33.1	3.7	36.8	0.4	3.8	4.1	5.7	1.7	7.4	3.6	8.5	12.1	8.3	1.6	10.0	0.4	0.0	0.4	13.6	5.6	19.2	4.8	3.3	8.1
Xylene	0.0	0.0	0.0	0.3	0.3	0.6	10.3	0.8	11.1	0.2	0.8	1.0	2.5	0.3	2.8	1.3	1.8	3.1	1.9	0.3	2.3	0.1	0.0	0.1	5.9	1.2	7.1	2.0	0.8	2.8
Aromatics	0.0	0.0	0.0	0.8	0.4	1.2	24.9	1.2	26.0	0.5	1.1	1.6	6.9	0.5	7.4	3.8	2.6	6.4	4.1	0.7	4.7	0.3	0.0	0.3	16.3	1.9	18.2	5.4	1.2	6.6
HCHO	0.0	0.0	0.0	0.1	5.4	5.4	3.6	17.9	21.5	0.1	17.4	17.5	0.9	8.4	9.4	0.4	43.1	43.6	0.8	10.8	11.6	0.4	0.0	0.4	2.2	29.5	31.6	0.7	17.5	18.2
Aldehydes	0.0	0.0	0.0	0.2	5.4	5.6	10.2	14.6	24.8	0.1	14.1	14.2	0.9	6.3	7.1	0.9	32.3	33.3	1.5	7.8	9.3	0.2	0.0	0.2	2.5	23.8	26.4	2.0	15.3	17.3
Ketones	0.0	0.0	0.0	0.0	10.4	10.4	3.1	28.3	31.4	0.0	27.3	27.3	0.6	12.2	12.8	0.3	63.0	63.3	1.2	15.5	16.7	0.2	0.0	0.2	1.1	46.5	47.6	0.2	29.8	30.0
es	0.1	0.0	0.1	0.0	0.4	0.5	3.6	0.7	4.3	0.0	0.6	0.6	1.1	0.2	1.3	0.3	1.3	1.6	1.4	0.7	2.1	0.8	0.0	0.8	1.5	1.6	3.2	0.2	1.4	1.6
Others	0.2	0.0	0.2	1.1	33.1	34.1	60.9	92.4	153.3	0.6	90.5	91.1	10.1	40.7	50.7	5.4	207.5	212.9	18.1	47.1	65.2	1.7	0.0	1.7	24.5	147.3	171.8	7.4	91.6	99.0

Table 1. continue (SouthAsia)

	Bangladesh			Bhutan			India			Nepal			Pakistan			Sri Lanka		
	Ant.	BB	Total	Ant.	BB	Total	Ant.	BB	Total	Ant.	BB	Total	Ant.	BB	Total	Ant.	BB	Total
SO_2	11.1	4.0	15.1	0.5	0.2	0.7	463.9	18.7	482.6	2.7	1.3	4.0	119.7	0.5	120.3	4.7	0.9	5.6
NO_x	13.4	27.1	40.5	0.4	1.1	1.6	343.7	137.6	481.3	2.1	6.9	9.0	40.6	5.5	46.1	4.0	4.1	8.1
CO	248.7	816.2	1064.9	8.2	25.9	34.1	4338.4	3101.3	7439.8	116.6	162.4	278.9	496.6	111.3	607.8	78.2	168.9	247.1
CH_4	268.5	37.6	306.1	3.2	1.1	4.4	2642.0	106.6	2748.6	76.7	6.5	83.2	450.7	3.5	454.2	27.9	10.8	38.7
NH_3	62.6	10.9	73.5	0.8	0.3	1.1	614.0	43.0	657.0	13.5	2.2	15.6	101.6	1.6	103.2	7.3	2.1	9.4
CO_2	7.9	13.0	20.9	0.2	0.4	0.6	143.3	50.4	193.7	2.4	2.5	4.9	17.0	2.0	18.9	1.9	2.6	4.4
BC	3.3	5.7	9.0	0.1	0.1	0.2	43.9	20.9	64.9	1.5	0.9	2.4	6.5	0.8	7.3	0.7	1.1	1.8
OC	15.9	34.6	50.6	0.5	2.2	2.7	186.0	163.9	349.8	7.0	11.9	18.9	26.8	4.7	31.5	2.8	8.3	11.2
PM_{10}	63.3	100.0	163.3	1.7	4.2	5.9	880.9	459.8	1340.7	22.5	25.8	48.2	128.2	15.7	143.9	18.2	17.3	35.5
$PM_{2.5}$	40.1	51.7	91.8	1.1	3.1	4.2	540.2	217.4	757.5	14.2	16.5	30.7	81.2	6.1	87.3	11.8	14.4	26.3
Ethane	3.3	9.9	13.2	0.1	0.2	0.3	47.1	29.0	76.0	1.5	1.2	2.7	6.4	1.1	7.5	0.9	2.1	3.1
Propane	1.4	3.3	4.7	0.0	0.1	0.1	26.7	14.7	41.4	0.4	0.5	1.0	4.2	0.6	4.8	0.4	0.3	0.7
Butane	1.6	0.6	2.2	0.1	0.0	0.1	41.5	2.7	44.1	0.4	0.1	0.5	6.7	0.1	6.7	1.1	0.1	1.2
Pentane	1.0	0.2	1.2	0.1	0.0	0.1	31.3	1.1	32.5	0.3	0.1	0.4	4.6	0.0	4.7	0.8	0.0	0.8
Oth.Alkane	3.4	2.1	5.5	0.2	0.1	0.2	74.9	7.8	82.7	1.0	0.4	1.4	11.5	0.3	11.7	1.9	0.4	2.3
Ethene	5.9	15.3	21.2	0.3	0.3	0.5	100.5	45.0	145.5	3.2	2.0	5.2	11.8	1.7	13.5	2.1	3.5	5.6
Propene	2.2	7.4	9.6	0.1	0.1	0.2	37.7	29.4	67.1	1.2	1.2	2.4	4.5	1.1	5.7	0.8	1.0	1.8
T. Alkene	1.4	4.5	5.9	0.1	0.2	0.3	24.9	17.7	42.6	0.7	1.1	1.8	3.1	0.6	3.6	0.5	1.0	1.6
I. Alkene	2.5	1.4	3.8	0.1	0.0	0.2	43.3	4.3	47.6	1.3	0.2	1.6	5.3	0.1	5.5	1.0	0.3	1.3
Acetylene	2.6	3.5	6.1	0.1	0.1	0.2	46.0	11.6	57.6	1.4	0.5	1.9	5.6	0.5	6.1	0.9	0.7	1.6
Benzene	2.6	2.3	4.9	0.1	0.1	0.2	41.1	8.5	49.5	1.4	0.6	2.0	4.8	0.2	5.0	0.8	0.7	1.5
Toluene	2.6	1.3	4.0	0.1	0.1	0.2	46.6	5.5	52.1	1.0	0.5	1.5	5.8	0.1	6.0	1.2	0.5	1.7
Xylene	0.8	0.3	1.1	0.0	0.0	0.1	19.3	2.2	21.5	0.4	0.2	0.6	2.2	0.0	2.3	0.5	0.1	0.6
Aromatics	1.8	0.8	2.6	0.1	0.0	0.2	45.5	4.1	49.5	0.9	0.3	1.2	5.7	0.1	5.8	1.2	0.2	1.4
HCHO	0.3	12.9	13.2	0.0	0.5	0.5	8.4	54.3	62.7	0.1	3.2	3.3	1.0	1.7	2.7	0.2	2.5	2.7
Aldehydes	1.1	9.2	10.2	0.0	0.3	0.3	16.8	34.6	51.5	0.6	1.8	2.4	2.0	1.3	3.3	0.4	1.9	2.2
Ketones	0.2	18.5	18.8	0.0	0.5	0.5	3.0	68.6	71.7	0.0	3.3	3.3	0.4	2.5	3.0	0.1	3.7	3.7
s	0.3	1.4	1.6	0.0	0.0	0.0	3.9	6.3	10.2	0.0	0.2	0.2	0.6	0.3	0.8	0.1	0.1	0.2
Others	6.3	50.4	56.6	0.2	2.6	2.7	81.6	213.1	294.7	1.7	14.4	16.1	11.0	6.5	17.5	1.9	12.1	14.1

Table 2. Observed and calculated values of parameters modeled by the CFORS/STEM-2K1 for TRACE-P DC-8 Flights #6 to #17.

Species and Variables	Below 1km			1km to 3km			Above 3km		
	Observed	Modeled	R	Observed	Modeled	R	Observed	Modeled	R
Wind Speed (m/s)	8.27	7.57	0.837	11.11	10.88	0.888	31.92	31.34	0.984
Temperature (K)	288.35	287.50	0.988	278.31	277.42	0.993	248.72	250.09	0.993
H_2O (ppmv)	1399.27	1408.63	0.983	6527.96	6977.35	0.961	1117.44	1534.05	0.906
CO (ppbv)	218.8	203.8	0.760	188.3	195.1	0.551	122.4	121.2	0.618
O_3 (ppbv)	51.06	51.32	0.811	52.822	52.88	0.733	61.44	59.92	0.278
Ethane (ppbv) *1	1.967	1.566	0.893	1.690	1.432	0.806	0.91	0.80	0.735
Propane (ppbv) *1	0.625	0.437	0.839	0.480	0.388	0.725	0.154	0.181	0.713
Ethyne (ppbv) *1	0.787	0.599	0.675	0.554	0.494	0.640	0.249	0.201	0.599
Ethene (ppbv) *1	0.179	0.148	0.678	0.114	0.109	0.367	0.033	0.025	0.479
SO_2 (ppbv)	1.557	0.990	0.676	0.677	0.994	0.271	0.192	0.095	0.677
SO_4 (ppbv)	1.586	1.35	0.680	0.827	1.059	0.493	0.218	0.202	0.722
Acetone (ppbv) *2	1.258	1.384	0.594	1.205	1.305	0.394	0.967	0.860	0.367
Acetone-Singh (ppbv) *3	0.941	1.384	0.544	0.931	1.305	0.459	0.686	0.860	0.564
PAN (ppbv)	0.545	0.501	0.808	0.314	0.440	0.667	0.188	0.127	0.552
NO_2 (ppbv)	0.267	0.307	0.236	0.120	0.300	0.305	0.034	0.007	0.075
NO (ppbv)	0.036	0.054	0.447	0.034	0.046	0.090	0.053	0.008	0.207
RNO_3 (ppbv) *1	0.046	0.067	0.828	0.031	0.050	0.796	0.012	0.014	0.732
Methyl Ethyl Ketone (ppbv) *2	0.236	0.210	0.576	0.193	0.181	0.374	0.077	0.071	0.513
H_2O_2 (ppbv)	0.845	1.051	0.544	1.105	1.160	0.564	0.433	0.491	0.550
Formaldehyde (ppbv) *4	0.596	0.622	0.686	0.328	0.468	0.401	0.097	0.125	0.608
Acetaldehyde (ppbv) *2	0.811	0.382	-0.238	0.545	0.348	-0.215	0.301	0.177	0.099
Acetaldehyde-Singh (ppbv) *3	0.480	0.382	0.581	0.315	0.348	0.438	0.141	0.177	0.607
OH (pptv)	0.108	0.097	0.608	0.107	0.125	0.816	0.114	0.133	0.690
HO_2 (pptv)	10.42	10.35	0.675	11.65	12.99	0.855	8.734	11.48	0.846
Benzene + Toluene (ppbv)	0.330	0.144	0.558	0.184	0.115	0.529	0.053	0.032	0.605
BC (ug/std m3) *5	0.840	0.694	0.631	0.836	0.586	0.228	0.258	0.165	0.348
AOE @550nm (/km) *5	0.0615	0.0722	0.642	0.0389	0.0528	0.342	0.0068	0.0086	0.575
$J[NO_2]$ (1/s)	1.95×10^{-5}	1.19×10^{-5}	0.839	2.78×10^{-5}	1.93×10^{-5}	0.86	4.15×10^{-5}	3.22×10^{-5}	0.933
$J[O_3\rightarrow O_2+O^1D]$ (1/s)	3.94×10^{-6}	2.84×10^{-6}	0.764	5.85×10^{-6}	4.85×10^{-6}	0.793	8.41×10^{-6}	7.73×10^{-6}	0.843
$J[H_2O_2]$ (1/s)	3.57×10^{-7}	2.47×10^{-7}	0.798	5.19×10^{-7}	4.09×10^{-7}	0.829	7.21×10^{-7}	6.37×10^{-7}	0.899
$J[HNO_3]$ (1/s)	1.21×10^{-3}	0.76×10^{-3}	0.741	1.81×10^{-3}	1.31×10^{-3}	0.743	2.58×10^{-3}	2.06×10^{-3}	0.73
$J[HNO_2\rightarrow OH+NO]$ (1/s)	1.75×10^{-5}	1.22×10^{-5}	0.77	2.68×10^{-5}	2.14×10^{-5}	0.798	4.36×10^{-5}	3.76×10^{-5}	0.862
$J[HCHO\rightarrow H+HCO]$ (1/s)	2.63×10^{-5}	1.77×10^{-5}	0.75	4.12×10^{-5}	3.11×10^{-5}	0.769	6.92×10^{-5}	5.22×10^{-5}	0.806
$J[HCHO\rightarrow H_2+CO]$ (1/s)	2.30×10^{-6}	2.02×10^{-6}	0.799	4.08×10^{-6}	4.05×10^{-6}	0.829	1.13×10^{-5}	1.19×10^{-5}	0.93
$J[CH3CHO\rightarrow CH_3+HCO]$ (1/s)	2.91×10^{-7}	2.47×10^{-7}	0.81	5.11×10^{-7}	4.87×10^{-7}	0.839	1.41×10^{-6}	1.42×10^{-6}	0.94
J[Acetone] (1/s)	1.95×10^{-5}	1.19×10^{-5}	0.839	2.78×10^{-5}	1.93×10^{-5}	0.86	4.15×10^{-5}	3.22×10^{-5}	0.933

*1: Ethane, propane, ethyne, ethene and RNO_3 presented here were measured by Blake and Atlas. Observed RNO_3 here is the sum of observed 2-$BuONO_2$, 2-$PeONO_2$, 3-$PeONO_2$, n-$PrONO_2$, i-$PrONO_2$, $MeONO_2$, and $EtONO_2$.
*2: Acetone, acetaldehyde and methyl ethyl ketone measured by Apel.

*3: Acetone and acetaldehyde measured by Singh
*4: Formaldehyde measured by Fried.
*5: The black carbon is derived from aerosol absorption. The aerosol extinction coefficient (AOE) is the sum of aerosol absorption at 565nm and aerosol scattering at 550nm

Table 3. Observed and calculated values of parameters modeled by the CFORS/STEM-2K1 for TRACE-P P-3B Flights #8 to #19

Species and Variables	Below 1km			1km to 3km			Above 3km		
	Observed	Modeled	R	Observed	Modeled	R	Observed	Modeled	R
Wind Speed (m/s)	10.75	9.41	0.88	10.25	10.26	0.913	17.65	17.88	0.95
Temperature (K)	287.15	286.07	0.988	279.96	278.42	0.986	266.442	266.25	0.991
H_2O (ppmv)	12646.1	12819.1	0.97	7594.4	7881.1	0.953	2651.9	3419.1	0.855
CO (ppbv)	235.326	219.507	0.712	208.143	209.861	0.527	136.073	148.625	0.752
O_3 (ppbv)	55.499	56.365	0.875	55.395	53.447	0.604	52.592	48.764	0.619
Ethane (ppbv)	2.192	1.749	0.699	1.675	1.534	0.635	1.109	1.051	0.766
Propane (ppbv)	0.731	0.515	0.725	0.429	0.418	0.584	0.210	0.248	0.713
Ethyne (ppbv)	0.792	0.686	0.682	0.597	0.544	0.392	0.302	0.277	0.487
Ethene (ppbv)	0.142	0.133	0.750	0.091	0.107	0.390	0.0328	0.0348	0.360
SO_2 (ppbv)	2.078	2.833	0.802	0.544	1.425	0.452	0.191	0.231	0.567
SO_4 (ppbv)	1.612	2.140	0.815	0.659	1.435	0.534	0.127	0.431	0.214
HNO_3 (ppbv)	0.378	0.886	0.216	0.265	0.718	0.230	0.168	0.156	0.314
PAN (ppbv)	0.536	0.659	0.781	0.374	0.519	0.649	0.190	0.181	0.712
NO_2 (ppbv)	0.431	0.413	0.091	0.404	0.247	0.373	0.035	0.011	0.312
NO (ppbv)	0.0798	0.077	0.066	0.0577	0.0531	0.172	0.0211	0.0068	0.357
RNO_3 (ppbv) *1	0.0558	0.0852	0.648	0.0306	0.0570	0.719	0.0149	0.0178	0.700
NO_y (ppbv)	1.648	2.501	0.689	1.385	1.905	0.433	0.510	0.485	0.597
Benzene + Toluene (ppbv)	0.283	0.153	0.637	0.209	0.116	0.417	0.0679	0.0424	0.455
OH (pptv)	0.213	0.114	0.540	0.196	0.160	0.832	0.172	0.138	0.850
HO_2 (pptv)	13.699	11.433	0.694	19.37	15.80	0.226	20.902	14.365	0.331
$HO_2 + RO_2$ (pptv)	21.213	19.011	0.759	34.882	26.147	0.718	27.087	25.171	0.630
AOE @550nm (/km) *2	0.0813	0.0936	0.529	0.0395	0.0586	0.299	0.0095	0.0187	0.413
$J[NO_2]$ (1/s)	0.00606	0.00481	0.70	0.0091	0.0081	0.734	0.0112	0.0103	0.705
$J[O_3 \rightarrow O_2+O^1D]$ (1/s)	1.89×10^{-5}	1.26×10^{-5}	0.803	3.42×10^{-5}	2.61×10^{-5}	0.868	4.12×10^{-5}	3.20×10^{-5}	0.911
$J[H_2O_2]$ (1/s)	4.21×10^{-6}	3.36×10^{-6}	0.716	6.85×10^{-6}	6.09×10^{-6}	0.793	8.45×10^{-6}	7.71×10^{-6}	0.812
$J[HNO_3]$ (1/s)	3.68×10^{-7}	2.80×10^{-7}	0.75	6.25×10^{-7}	5.31×10^{-7}	0.834	7.52×10^{-7}	6.56×10^{-7}	0.873
$J[HNO_2 \rightarrow OH+NO]$ (1/s)	1.33×10^{-3}	0.93×10^{-3}	0.70	2.01×10^{-3}	1.58×10^{-3}	0.738	2.51×10^{-3}	2.02×10^{-3}	0.71
$J[HCHO \rightarrow H+HCO]$ (1/s)	1.85×10^{-5}	1.44×10^{-5}	0.723	3.14×10^{-5}	2.71×10^{-5}	0.802	4.09×10^{-5}	3.56×10^{-5}	0.819
$J[HCHO \rightarrow H_2+CO]$ (1/s)	2.86×10^{-5}	2.14×10^{-5}	0.705	4.72×10^{-5}	3.84×10^{-5}	0.773	6.34×10^{-5}	5.02×10^{-5}	0.761
$J[CH3CHO \rightarrow CH_3+HCO]$ (1/s)	2.35×10^{-6}	2.29×10^{-6}	0.748	4.92×10^{-6}	5.29×10^{-6}	0.848	8.08×10^{-6}	8.54×10^{-6}	0.88
J[Acetone] (1/s)	2.91×10^{-7}	2.73×10^{-7}	0.761	6.18×10^{-7}	6.43×10^{-7}	0.856	1.01×10^{-6}	1.02×10^{-6}	0.892

*1: Observed RNO_3 here is the sum of observed 2-$BuONO_2$, 2-$PeONO_2$, 3-$PeONO_2$, n-$PrONO_2$, i-$PrONO_2$, $MeONO_2$, and $EtONO_2$, measured by Blake and Atlas.
*2: The aerosol extinction coefficient (AOE) is the sum of aerosol absorption at 565nm and aerosol scattering at 550nm.

Table 4. Ozone production efficiencies (O_3/NO_z) estimated from the aircraft observations using regional classification based on back trajectory analysis.

Region	**O_3/NO_z**
Biomass Burning (SEAsia)	16.2
Philippine	38.1
South China	15.1
Middle China	3.4
N. China, Korea	0.8
Japan	16.3

CFORS/STEM-2K1 Model Data Flow Chart

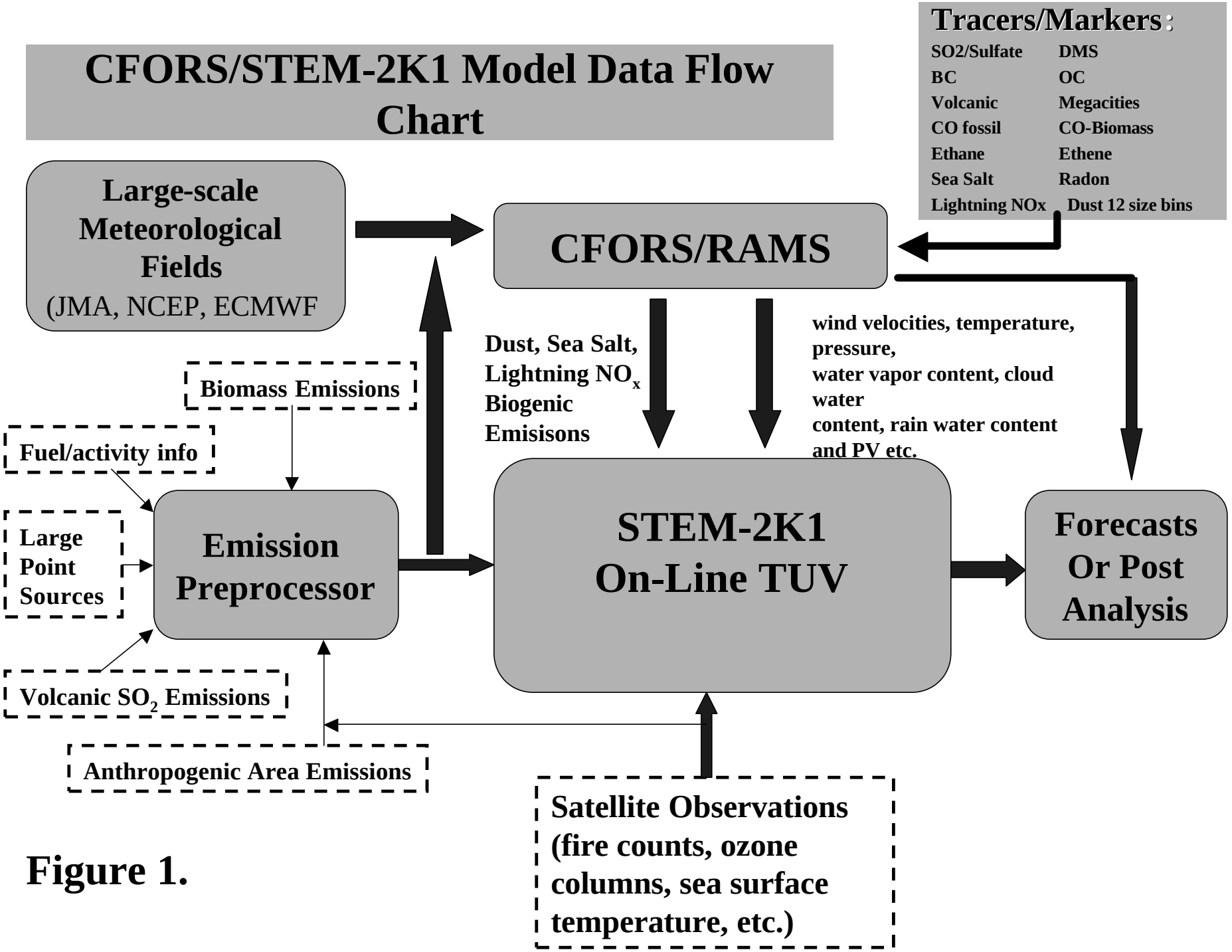

Figure 1.

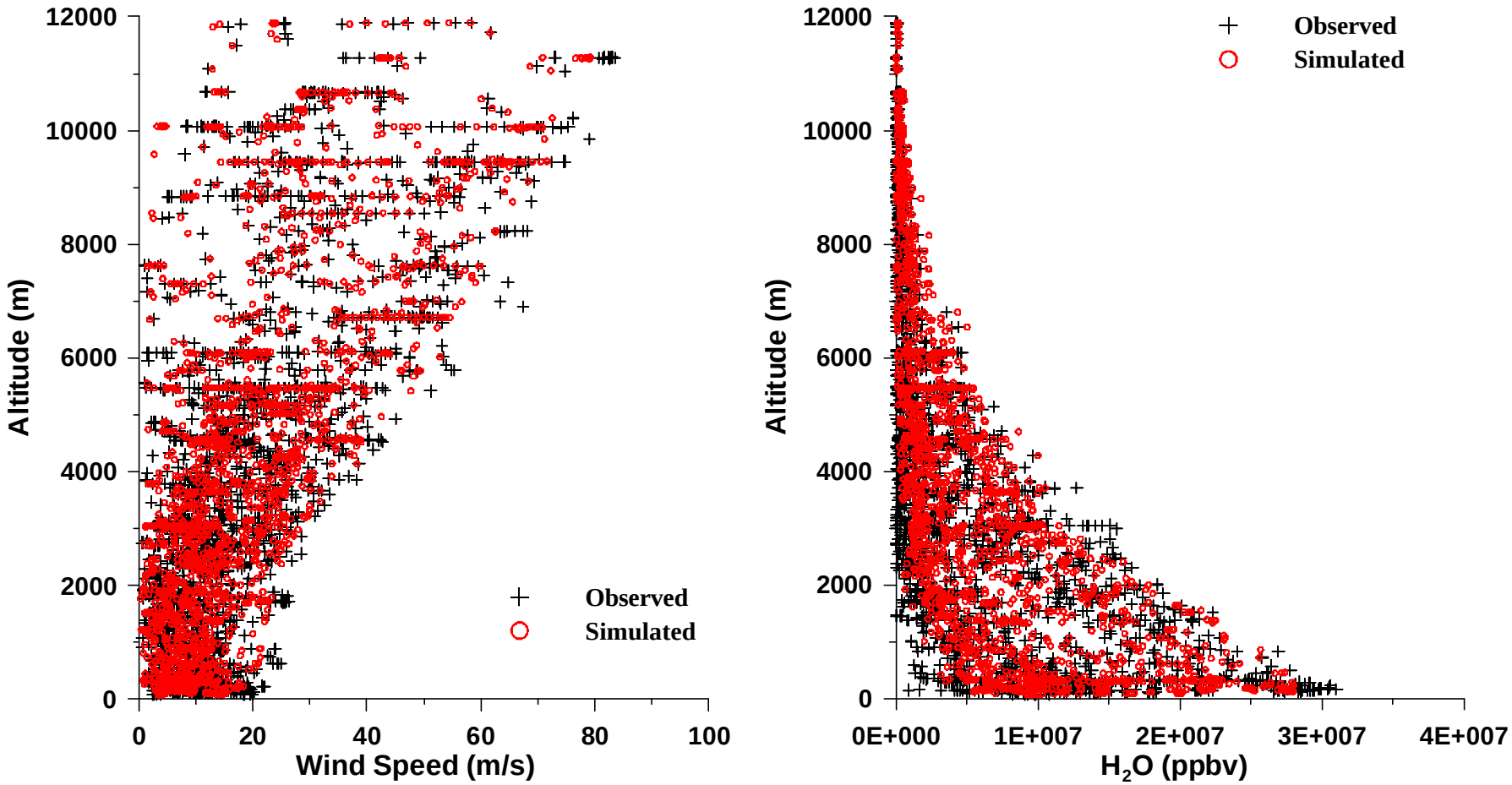
Altitude (m)
Wind Speed (m/s)
Observed
Simulated
Altitude (m)
H2O (ppbv)
Observed
Simulated

Figure 2

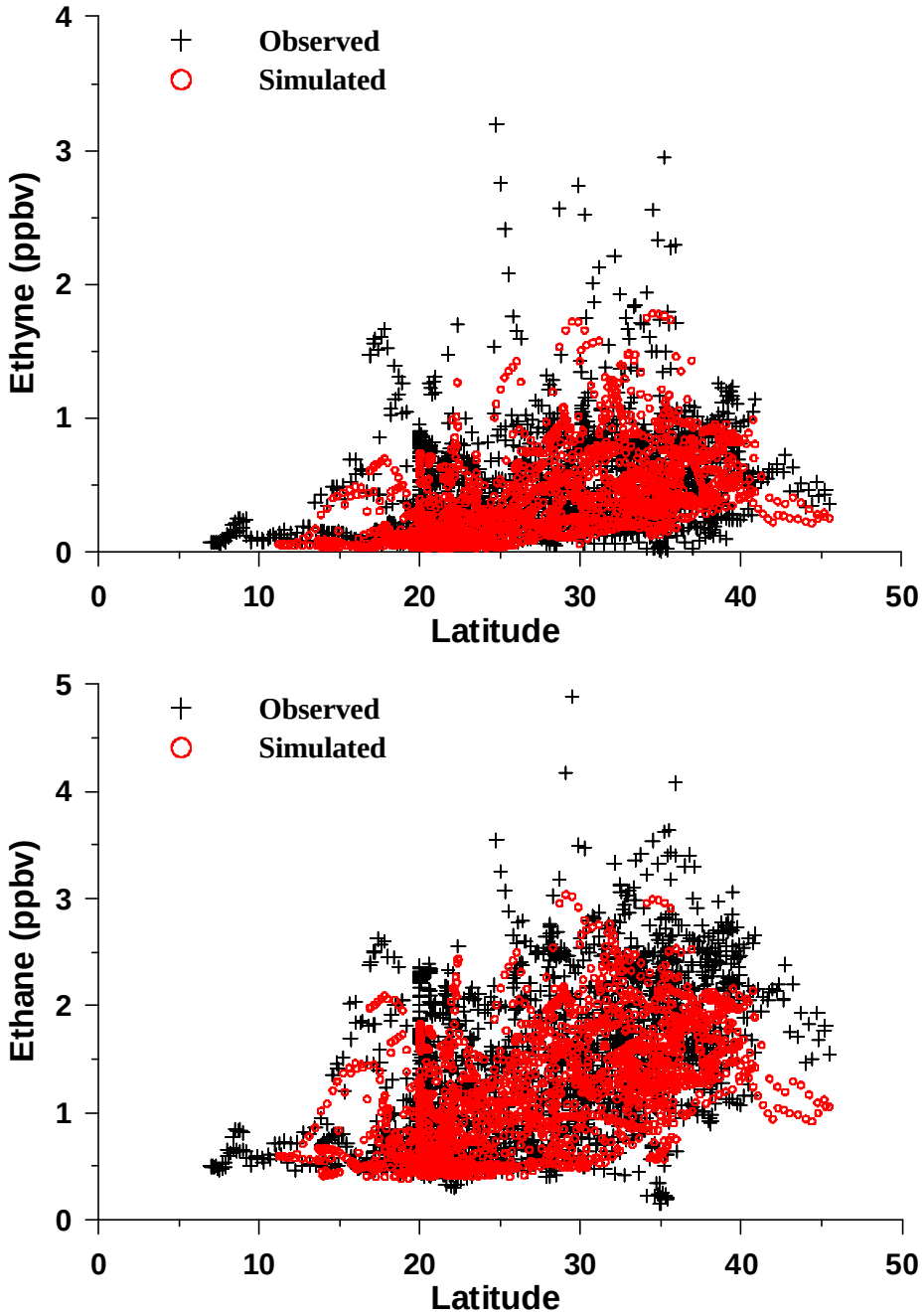
Observed
Simulated
Ethyne (ppbv)
Latitude
0
1
2
3
4
0
10
20
30
40
50
Observed
Simulated
Ethane (ppbv)
Latitude
0
1
2
3
4
5
0
10
20
30
40
50

Figure 3.

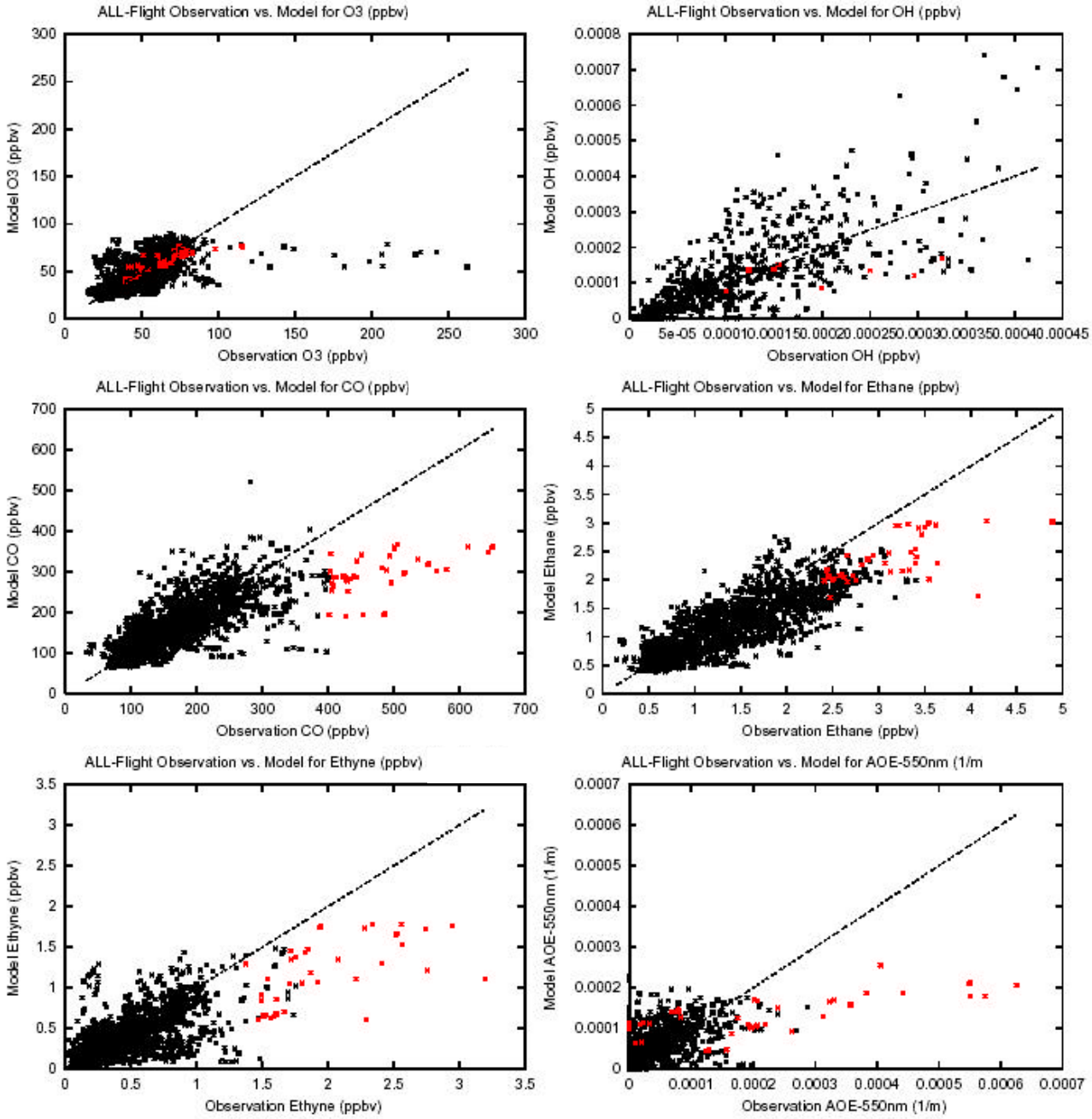
ALL-Flight Observation vs. Model for O3 (ppbv)
Model O3 (ppbv)
Observation O3 (ppbv)
ALL-Flight Observation vs. Model for OH (ppbv)
Model OH (ppbv)
Observation OH (ppbv)
ALL-Flight Observation vs. Model for CO (ppbv)
Model CO (ppbv)
Observation CO (ppbv)
ALL-Flight Observation vs. Model for Ethane (ppbv)
Model Ethane (ppbv)
Observation Ethane (ppbv)
ALL-Flight Observation vs. Model for Ethyne (ppbv)
Model Ethyne (ppbv)
Observation Ethyne (ppbv)
ALL-Flight Observation vs. Model for AOE-550nm (1/m
Model AOE-550nm (1/m)
Observation AOE-550nm (1/m)

Figure 4

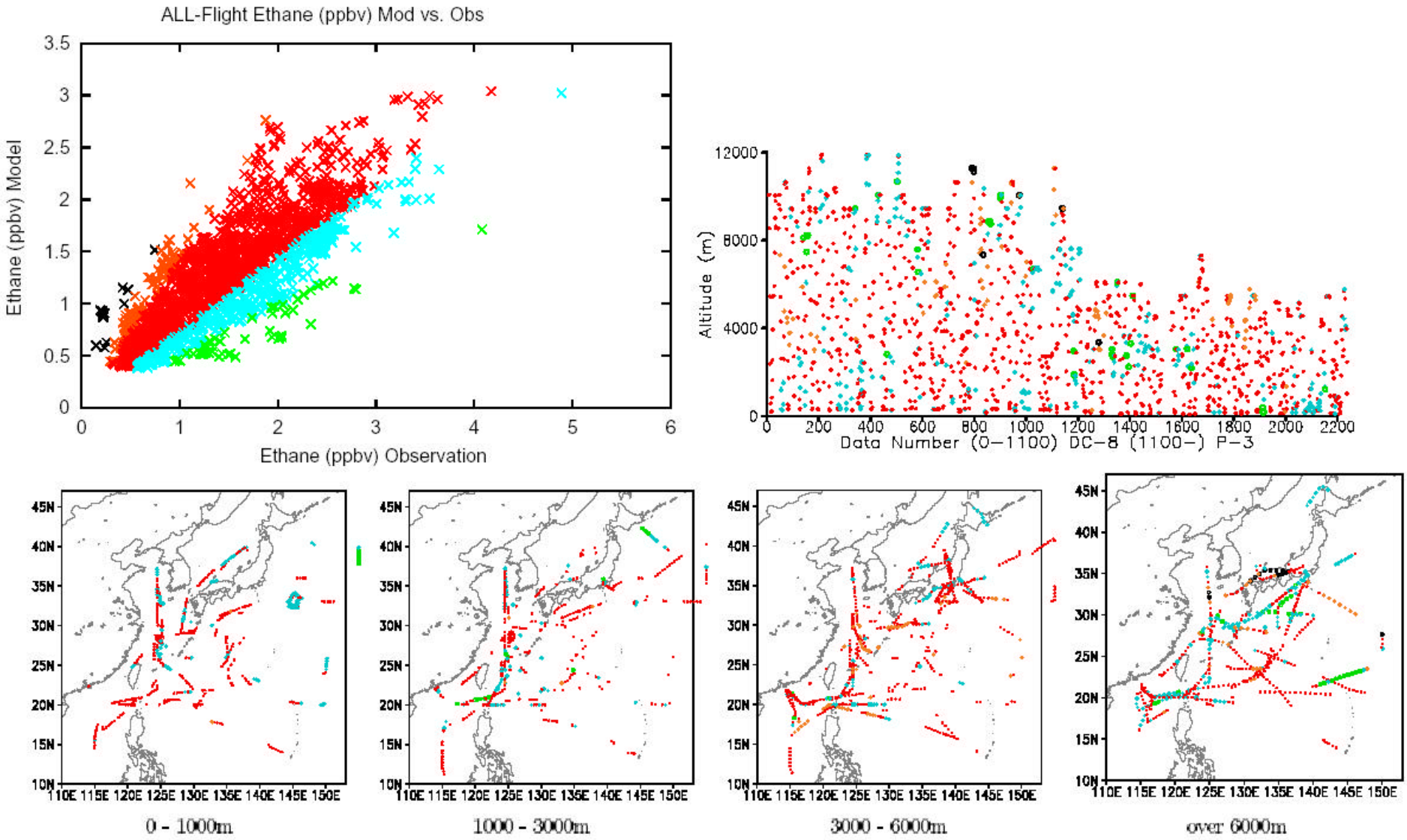
ALL-Flight Ethane (ppbv) Mod vs. Obs
Ethane (ppbv) Model
Ethane (ppbv) Observation
Altitude (m)
Data Number (0–1100) DC-8 (1100–) P-3
0 - 1000m
1000 - 3000m
3000 - 6000m
over 6000m

Figure 5

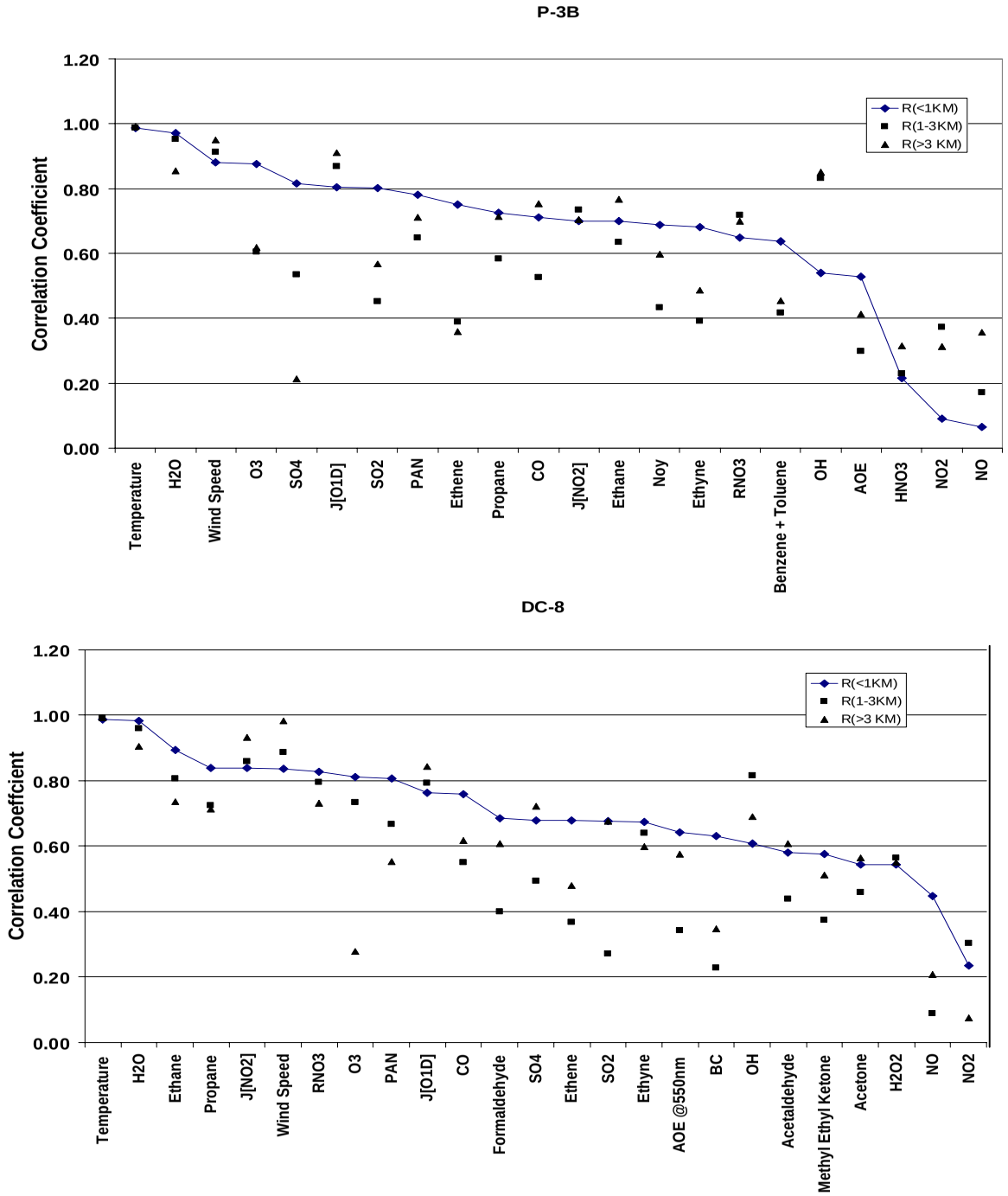
P-3B
Correlation Coefficient
1.20
1.00
0.80
0.60
0.40
0.20
0.00
R(<1KM)
R(1-3KM)
R(>3 KM)
Temperature
H2O
Wind Speed
O3
SO4
J[O1D]
SO2
PAN
Ethene
Propane
CO
J[NO2]
Ethane
Noy
Ethyne
RNO3
Benzene + Toluene
OH
AOE
HNO3
NO2
NO
DC-8
Correlation Coefficient
1.20
1.00
0.80
0.60
0.40
0.20
0.00
R(<1KM)
R(1-3KM)
R(>3 KM)
Temperature
H2O
Ethane
Propane
J[NO2]
Wind Speed
RNO3
O3
PAN
J[O1D]
CO
Formaldehyde
SO4
Ethene
SO2
Ethyne
AOE @550nm
BC
OH
Acetaldehyde
Methyl Ethyl Ketone
Acetone
H2O2
NO
NO2

Figure 6

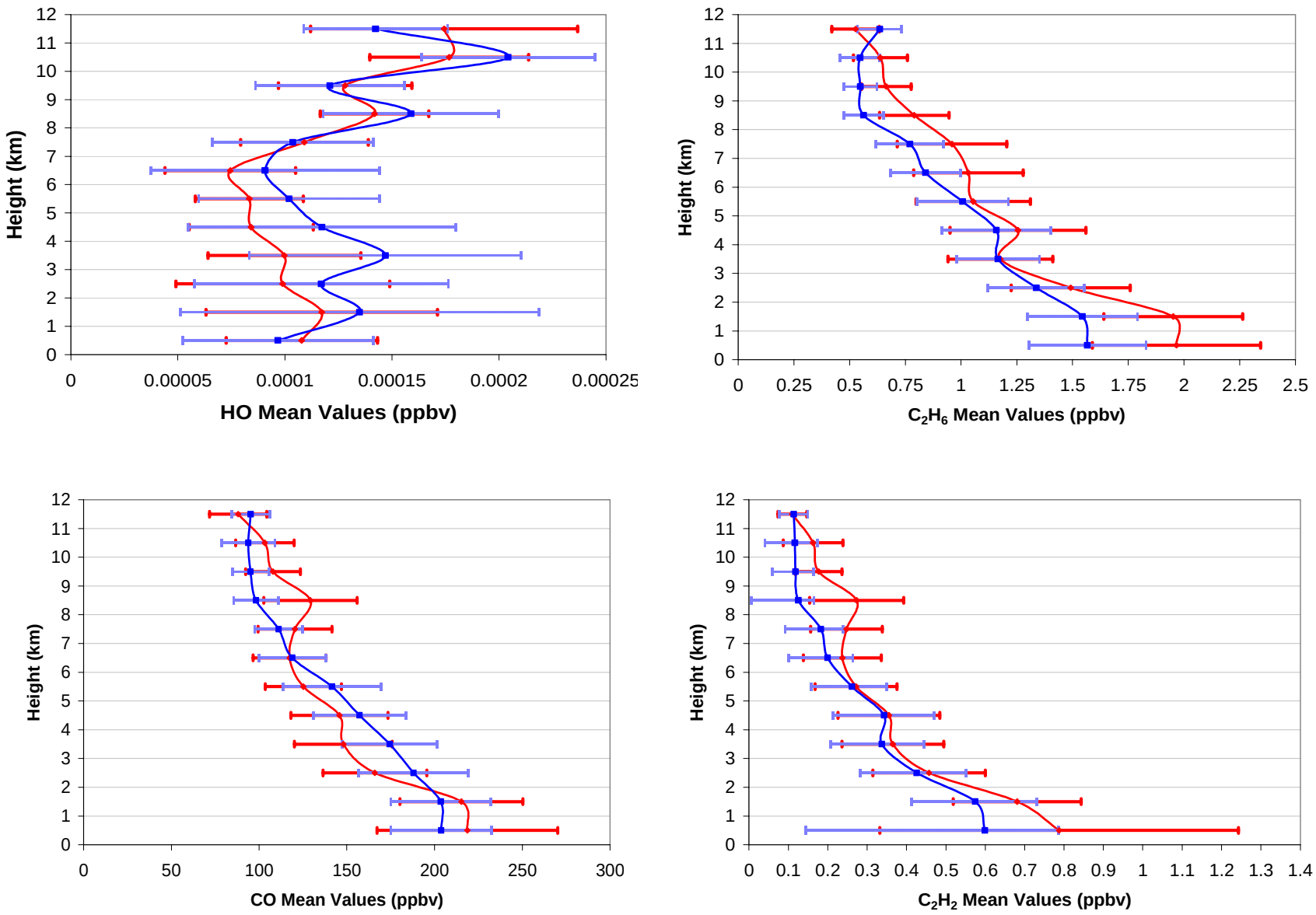
Height (km)
HO Mean Values (ppbv)
0
0.00005
0.0001
0.00015
0.0002
0.00025
C_2H_6 Mean Values (ppbv)
0
0.25
0.5
0.75
1
1.25
1.5
1.75
2
2.25
2.5
CO Mean Values (ppbv)
0
50
100
150
200
250
300
C_2H_2 Mean Values (ppbv)
0
0.1
0.2
0.3
0.4
0.5
0.6
0.7
0.8
0.9
1
1.1
1.2
1.3
1.4

Figure 7

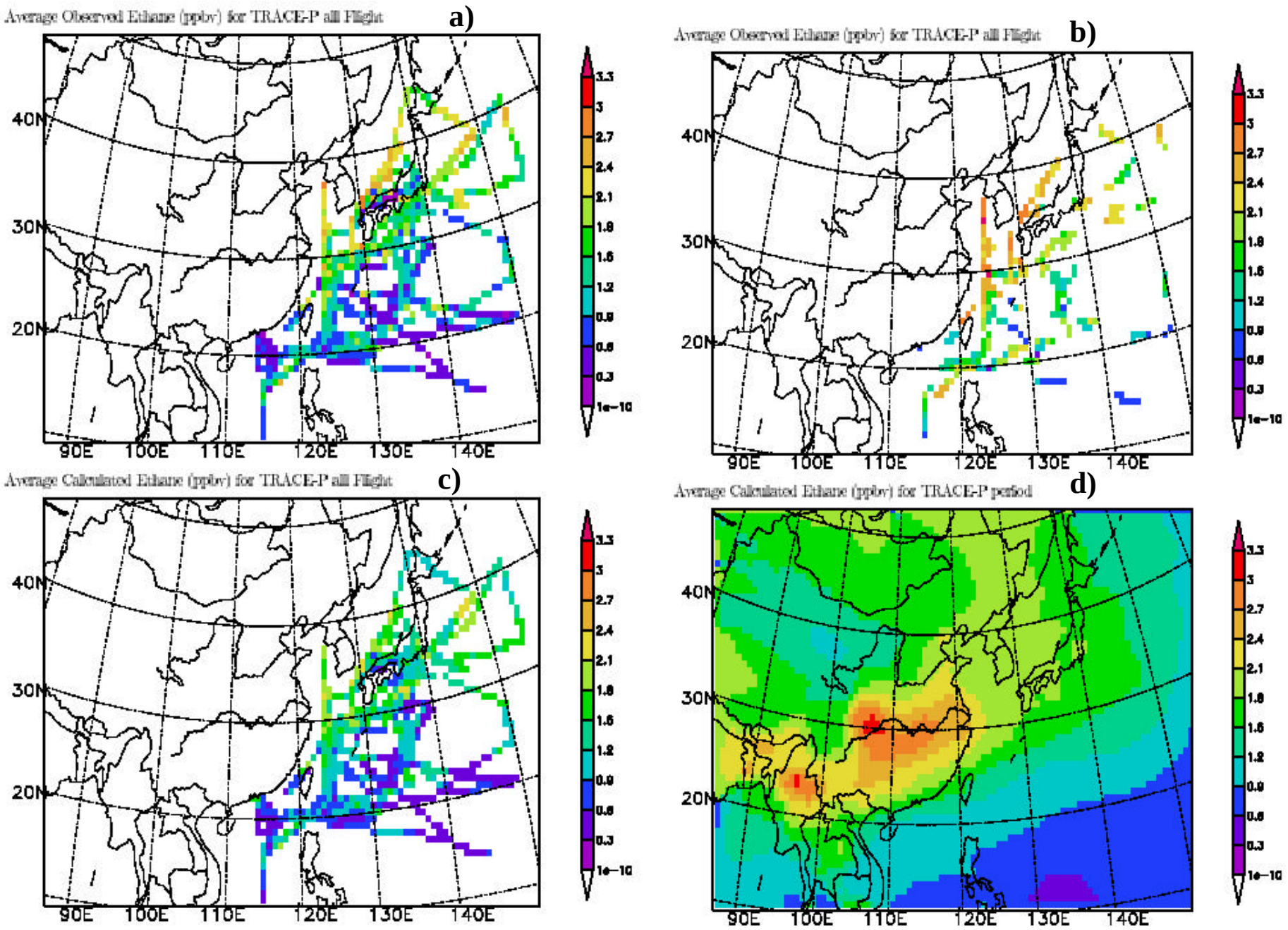
a)
Average Observed Ethane (ppbv) for TRACE-P all Flight
b)
Average Observed Ethane (ppbv) for TRACE-P all Flight
c)
Average Calculated Ethane (ppbv) for TRACE-P all Flight
d)
Average Calculated Ethane (ppbv) for TRACE-P period
40N
30N
20N
90E
100E
110E
120E
130E
140E
3.3
3
2.7
2.4
2.1
1.8
1.5
1.2
0.9
0.6
0.3
1e-10

Figure 8

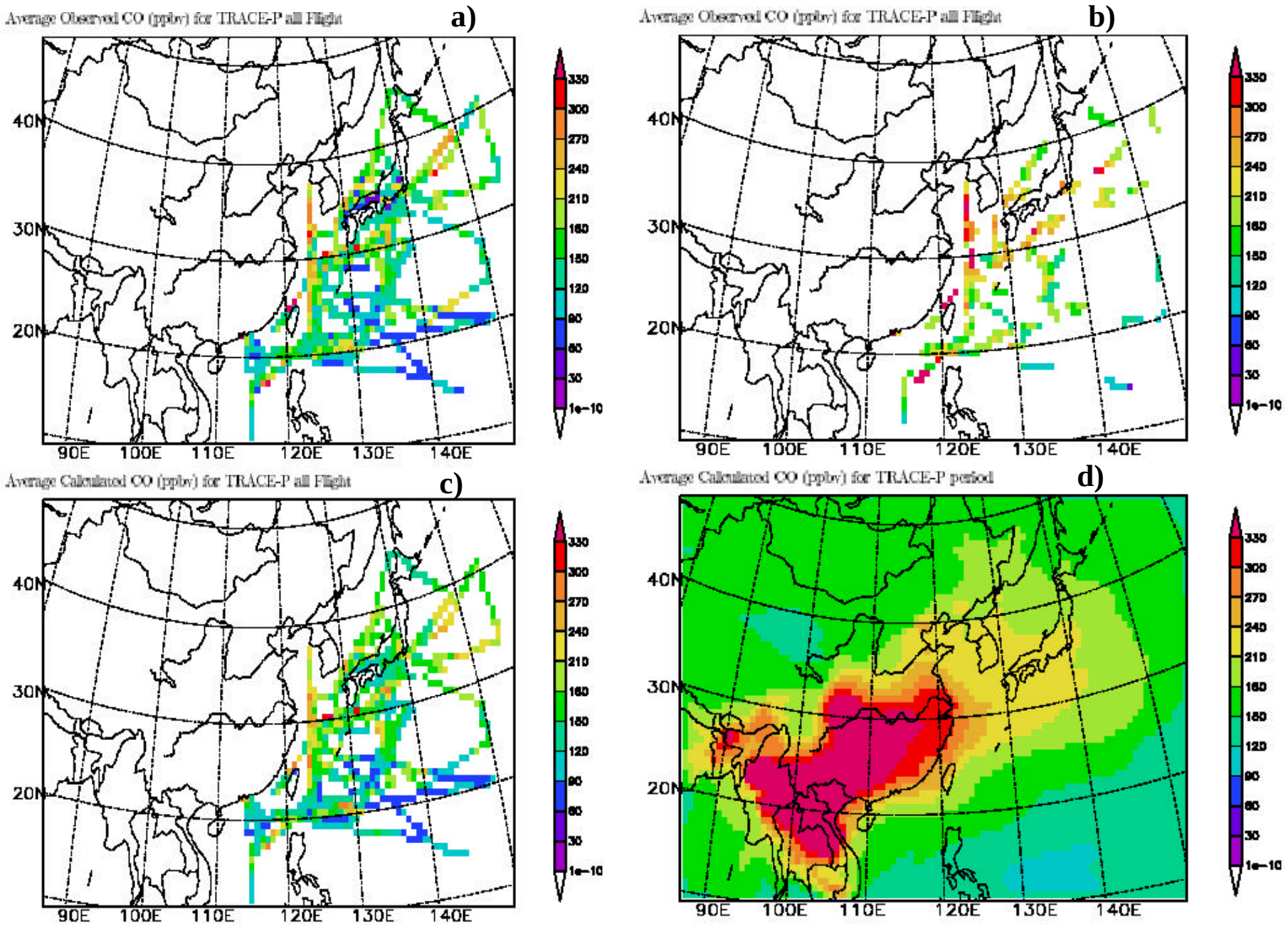
Average Observed CO (ppbv) for TRACE-P all Flight
a)
Average Observed CO (ppbv) for TRACE-P all Flight
b)
Average Calculated CO (ppbv) for TRACE-P all Flight
c)
Average Calculated CO (ppbv) for TRACE-P period
d)
40N
30N
20N
90E
100E
110E
120E
130E
140E
330
300
270
240
210
180
150
120
90
60
30
1e-10

Figure 9

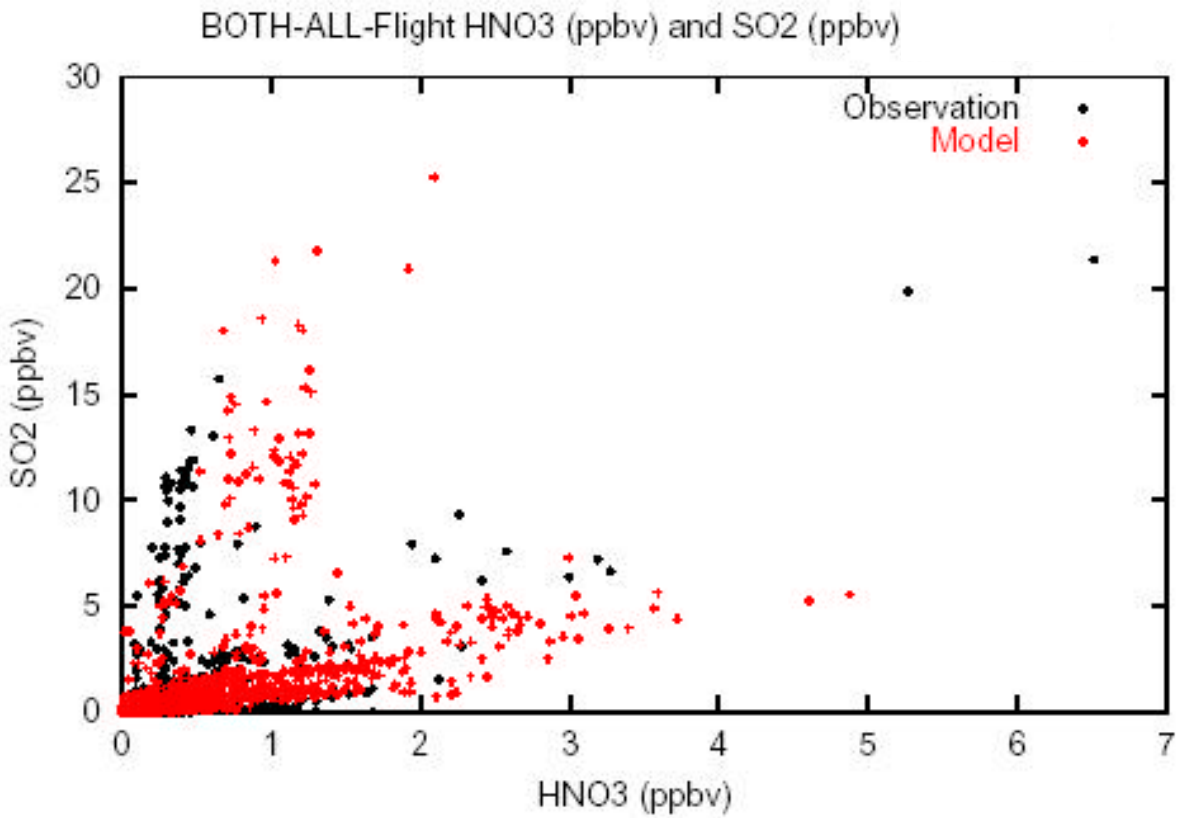
BOTH-ALL-Flight HNO3 (ppbv) and SO2 (ppbv)
Observation
Model
SO2 (ppbv)
HNO3 (ppbv)
0
5
10
15
20
25
30
0
1
2
3
4
5
6
7

Figure 10

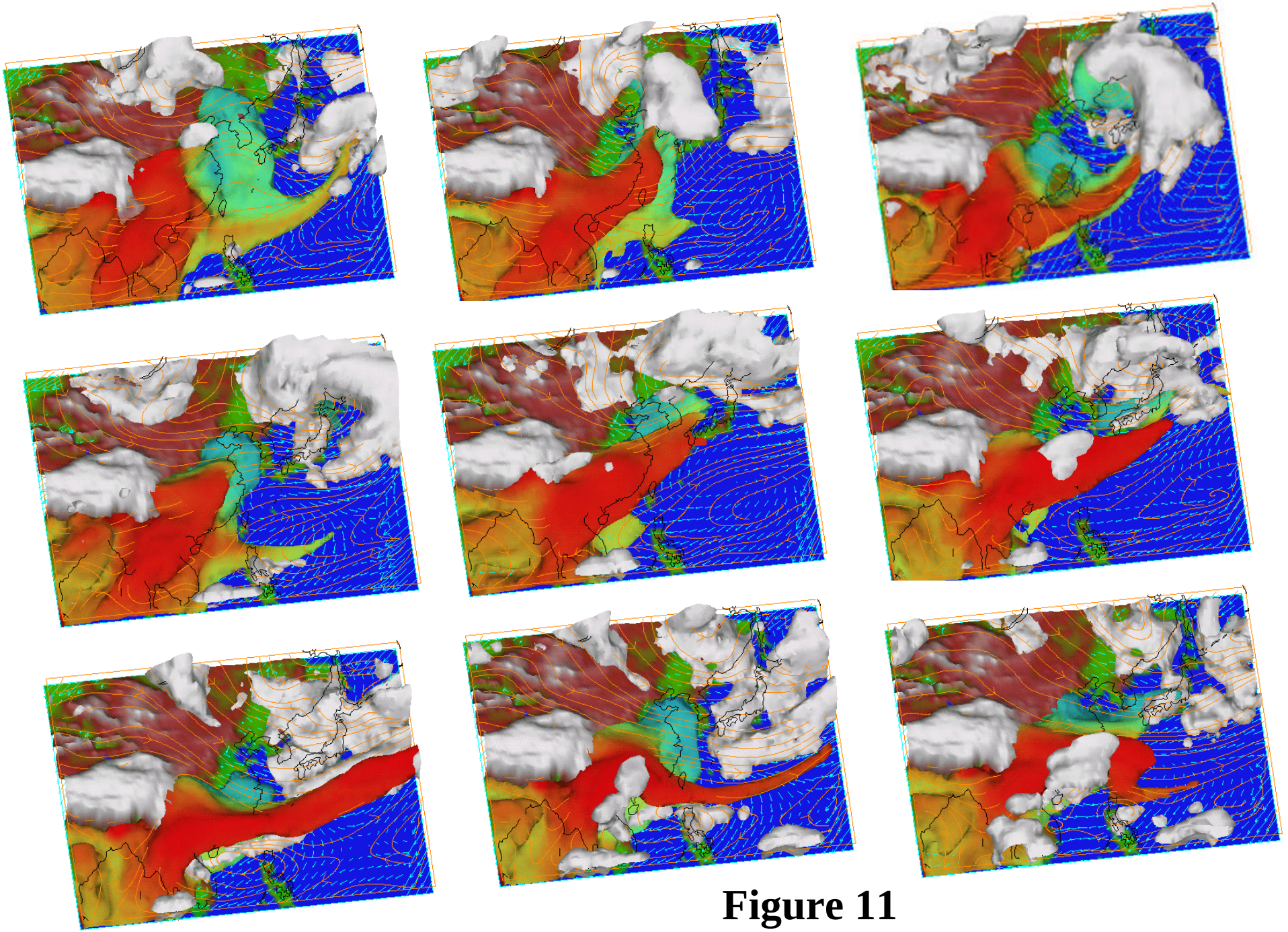

Figure 11

Figure 12

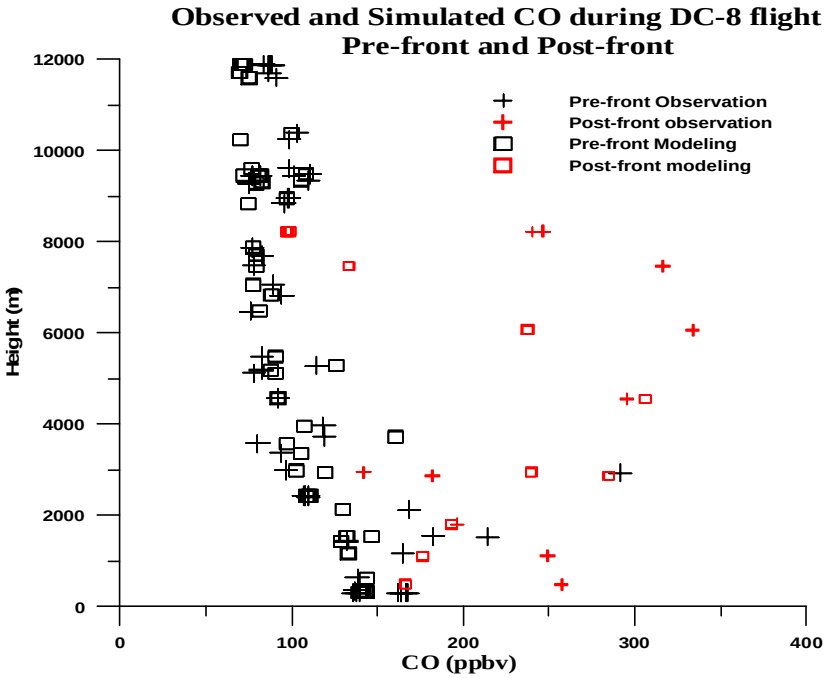
Observed and Simulated CO during DC-8 flight 7
Pre-front and Post-front
Pre-front Observation
Post-front observation
Pre-front Modeling
Post-front modeling
Height (m)
CO (ppbv)
0
2000
4000
6000
8000
10000
12000
0
100
200
300
400

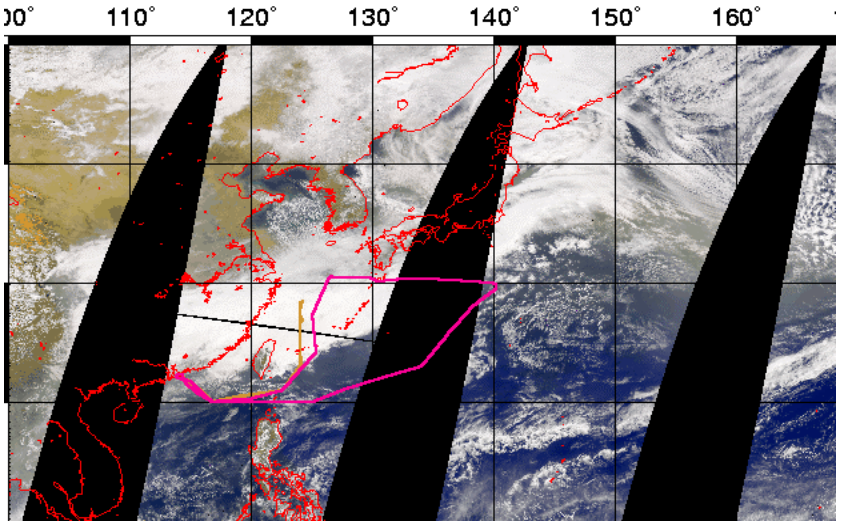
110°
120°
130°
140°
150°
160°

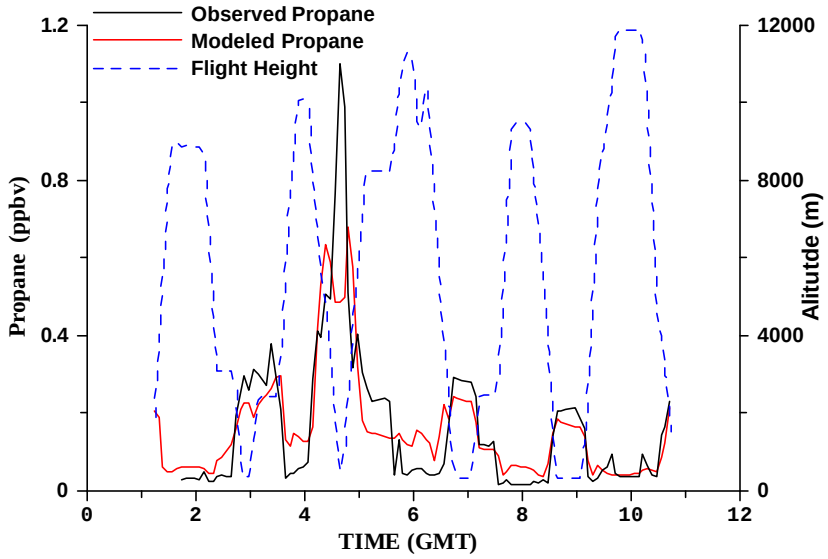
Simulated Propane Compared to DC-8 Observation Flight #7 (03/07/2001)
Observed Propane
Modeled Propane
Flight Height
Propane (ppbv)
Alitutde (m)
TIME (GMT)
0
0.4
0.8
1.2
0
4000
8000
12000
0
2
4
6
8
10
12

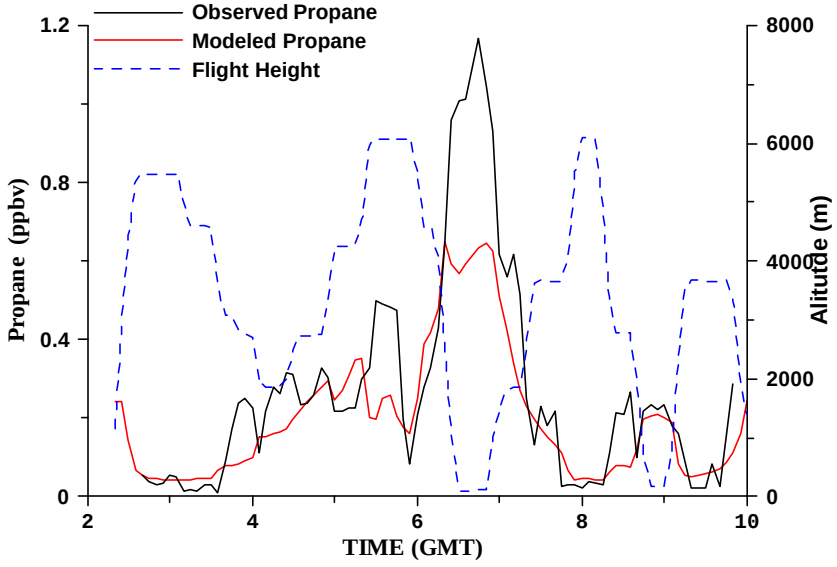
Simulated Propane Compared to P-3B Observation Flight #9 (03/07/2001)
Observed Propane
Modeled Propane
Flight Height
Propane (ppbv)
Alitutde (m)
TIME (GMT)
0
0.4
0.8
1.2
0
2000
4000
6000
8000
2
4
6
8
10

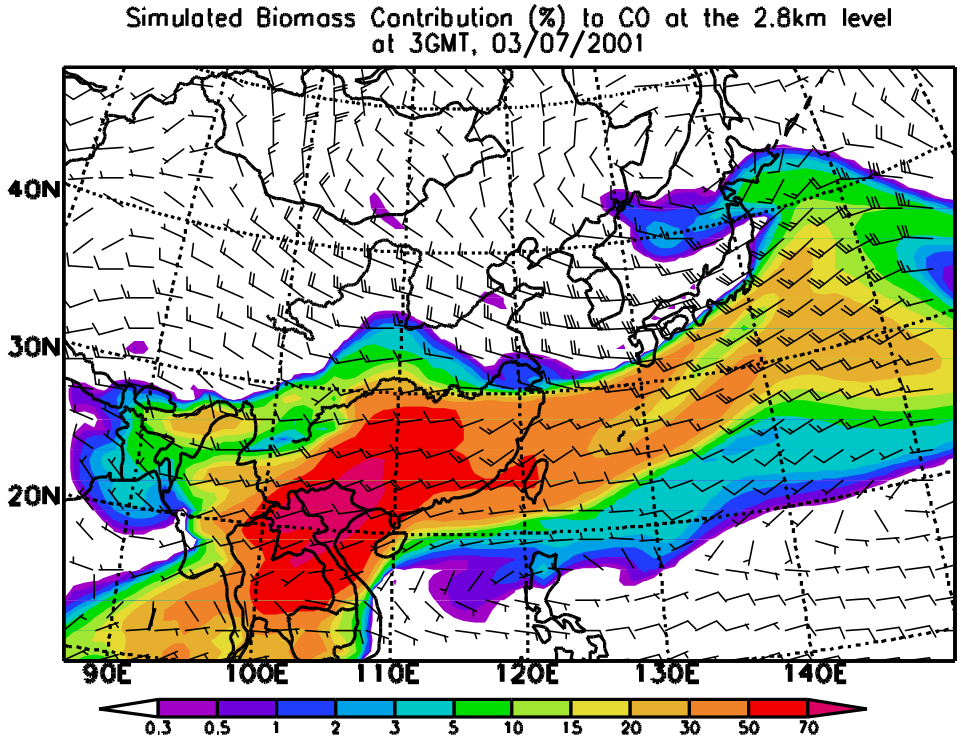
Simulated Biomass Contribution (%) to CO at the 2.8km level
at 3GMT, 03/07/2001
40N
30N
20N
90E
100E
110E
120E
130E
140E
0.3
0.5
1
2
3
5
10
15
20
30
50
70

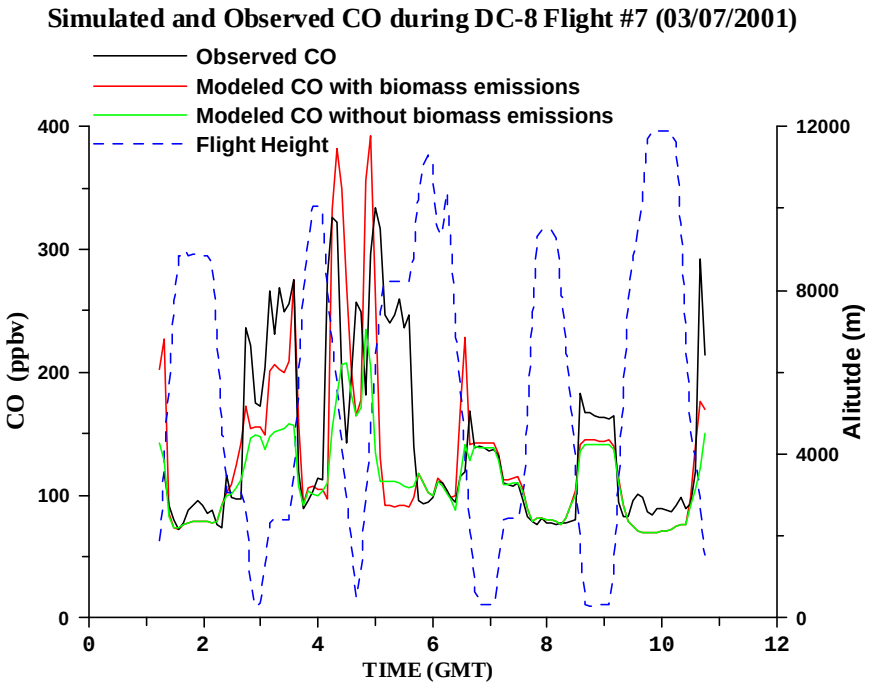
Simulated and Observed CO during DC-8 Flight #7 (03/07/2001)
Observed CO
Modeled CO with biomass emissions
Modeled CO without biomass emissions
Flight Height
CO (ppbv)
Alitutde (m)
TIME (GMT)
0
100
200
300
400
0
4000
8000
12000
0
2
4
6
8
10
12

Figure 13

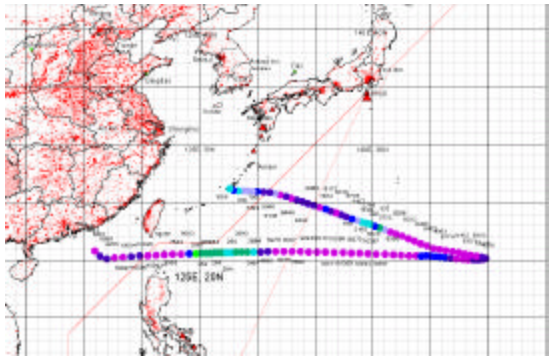

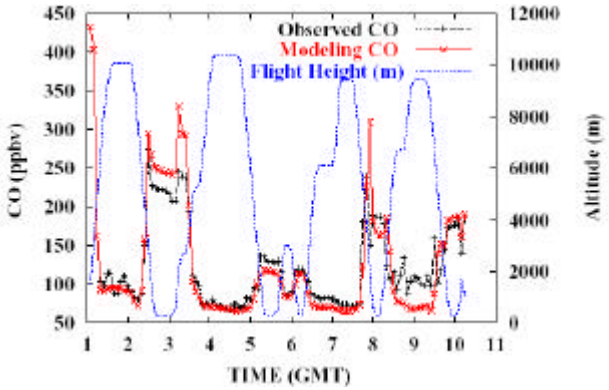
Observed CO
Modeling CO
Flight Height (m)
CO (ppbv)
Altitude (m)
TIME (GMT)

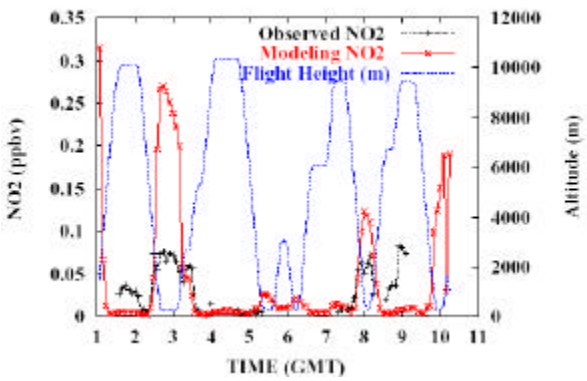
Observed NO2
Modeling NO2
Flight Height (m)
NO2 (ppbv)
Altitude (m)
TIME (GMT)

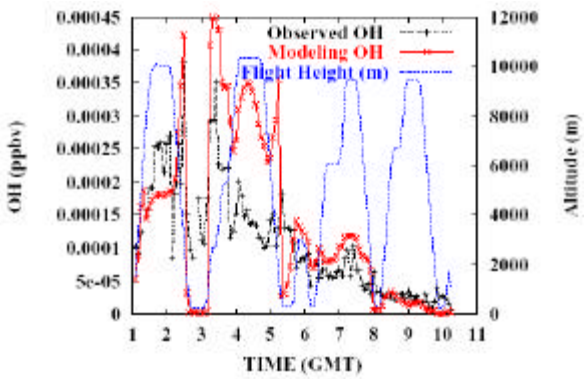
Observed OH
Modeling OH
Flight Height (m)
OH (ppbv)
Altitude (m)
TIME (GMT)

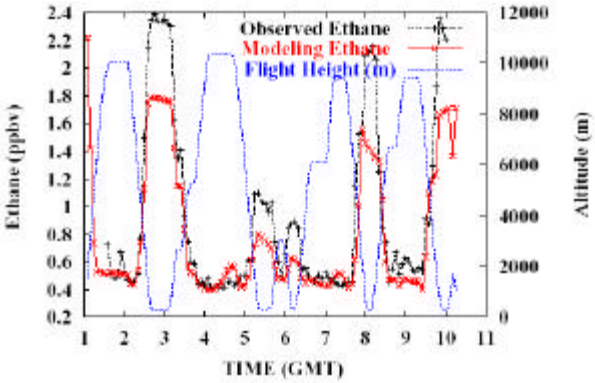
Observed Ethane
Modeling Ethane
Flight Height (m)
Ethane (ppbv)
Altitude (m)
TIME (GMT)

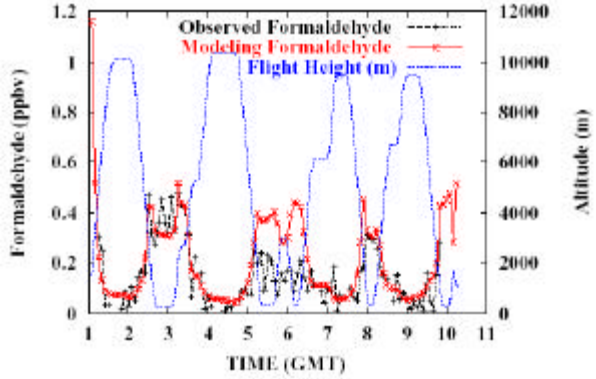
Observed Formaldehyde
Modeling Formaldehyde
Flight Height (m)
Formaldehyde (ppbv)
Altitude (m)
TIME (GMT)

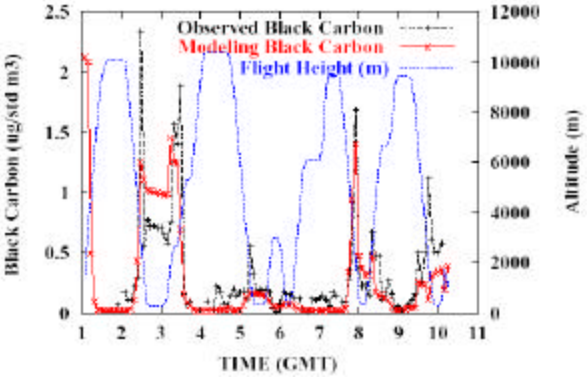
Observed Black Carbon
Modeling Black Carbon
Flight Height (m)
Black Carbon (ug/std m3)
Altitude (m)
TIME (GMT)

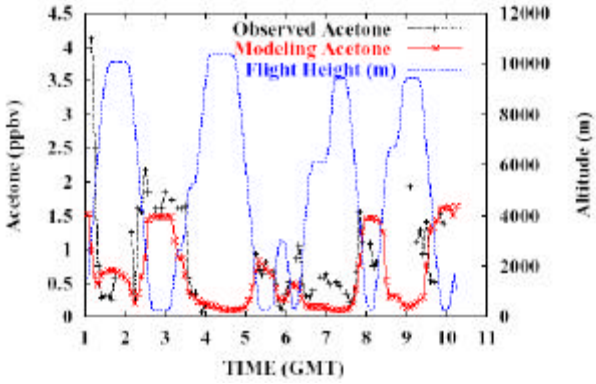
Observed Acetone
Modeling Acetone
Flight Height (m)
Acetone (ppbv)
Altitude (m)
TIME (GMT)

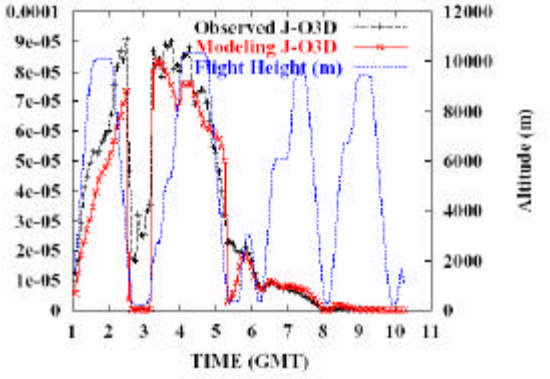
Observed J-O3D
Modeling J-O3D
Flight Height (m)
J-O3D (1/s)
Altitude (m)
TIME (GMT)

Figure 14

Frontal outflow of biomass burning plumes E of Hong Kong

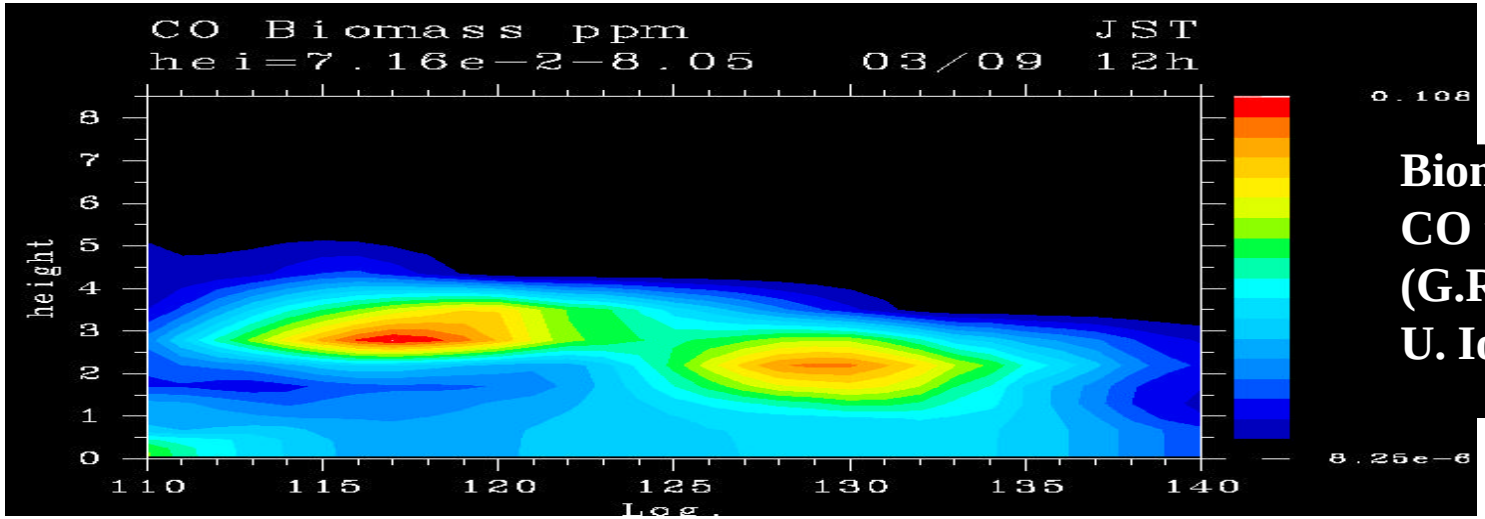

Biomass burning CO forecast (G.R. Carmichael, U. Iowa)

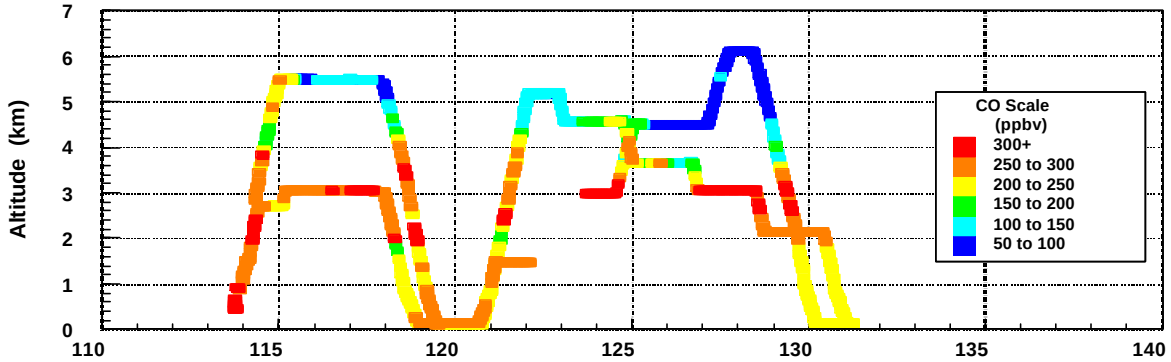

Observed CO (G.W. Sachse, NASA/LaRC)

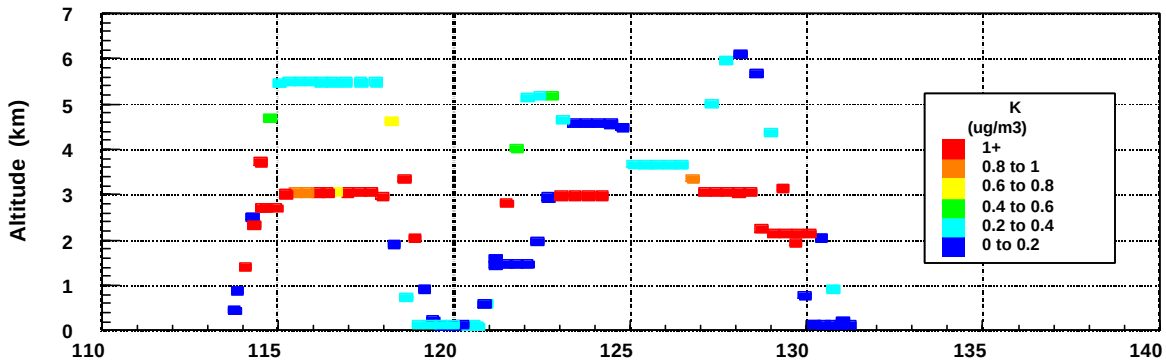

Observed aerosol potassium (R. Weber, Georgia Tech)

Figure 15

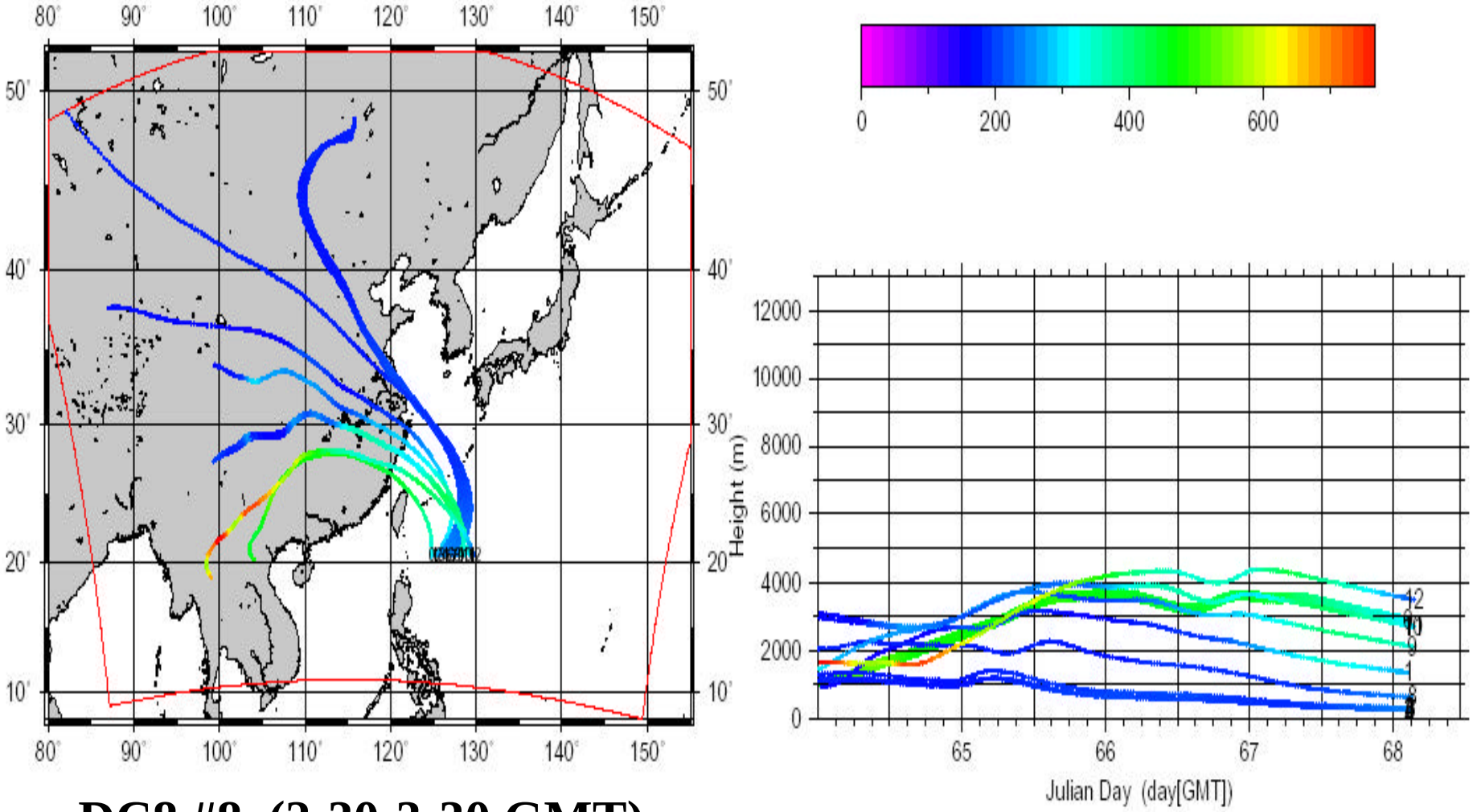

DC8 #8 (2:30-3:30 GMT)

Figure 16

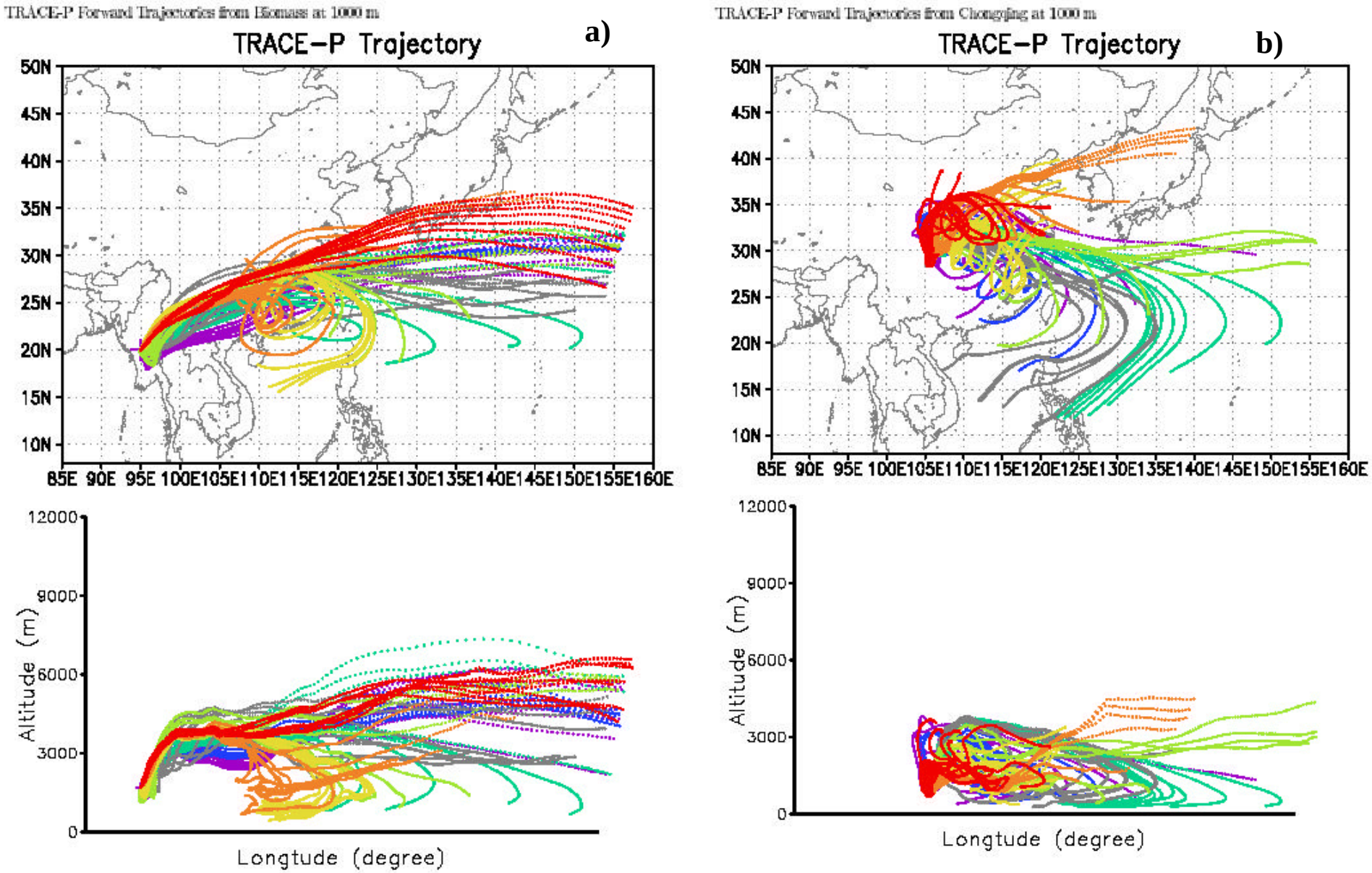
TRACE-P Forward Trajectories from Hanoi at 1000 m
TRACE-P Trajectory
a)
50N
45N
40N
35N
30N
25N
20N
15N
10N
85E 90E 95E 100E105E110E115E120E125E130E135E140E145E150E155E160E
12000
9000
6000
3000
0
Altitude (m)
Longtude (degree)
TRACE-P Forward Trajectories from Chongqing at 1000 m
TRACE-P Trajectory
b)
50N
45N
40N
35N
30N
25N
20N
15N
10N
85E 90E 95E 100E105E110E115E120E125E130E135E140E145E150E155E160E
12000
9000
6000
3000
0
Altitude (m)
Longtude (degree)
3 4 5 6 7 8 9 10
Day of March

Figure 17

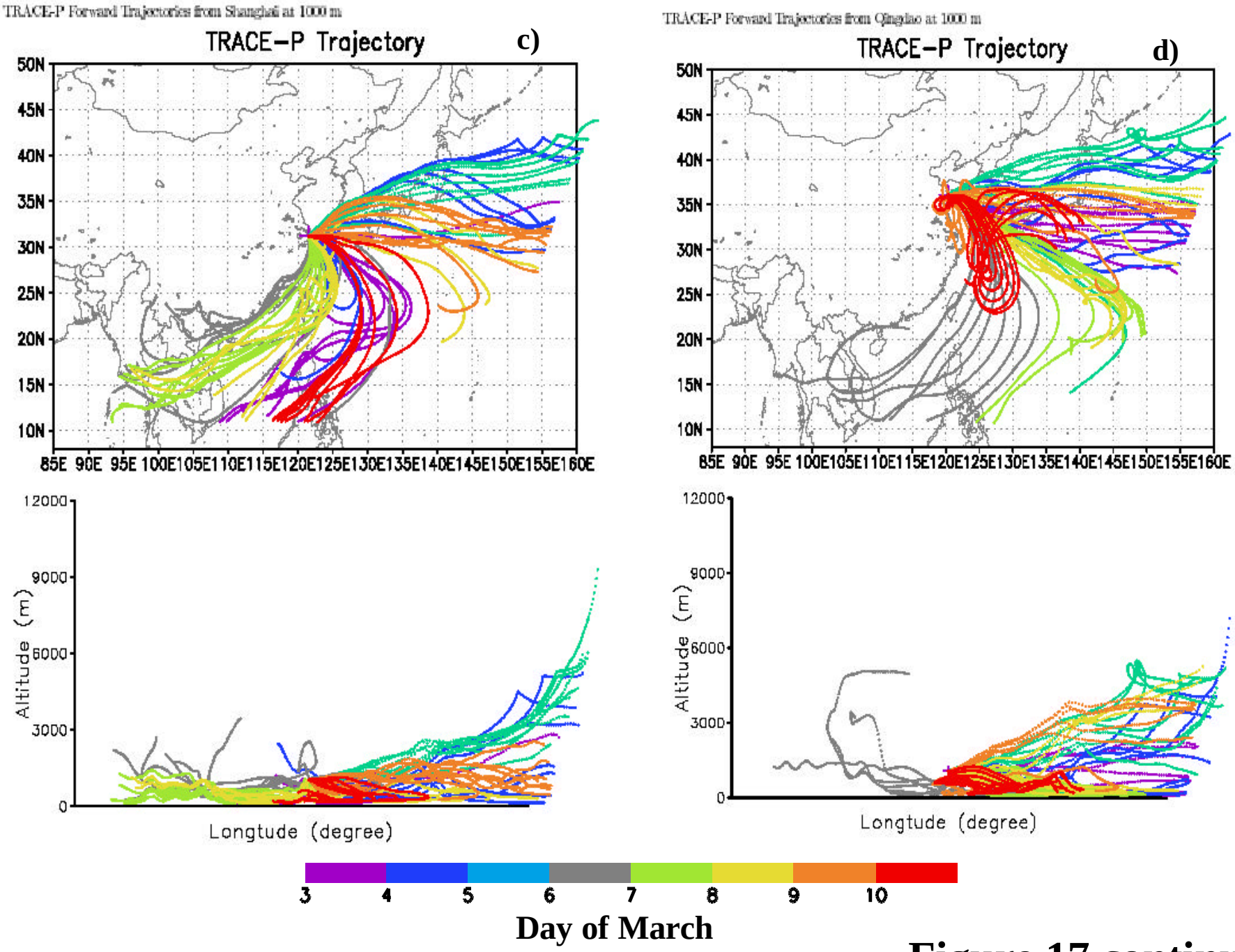

Figure 17 continued

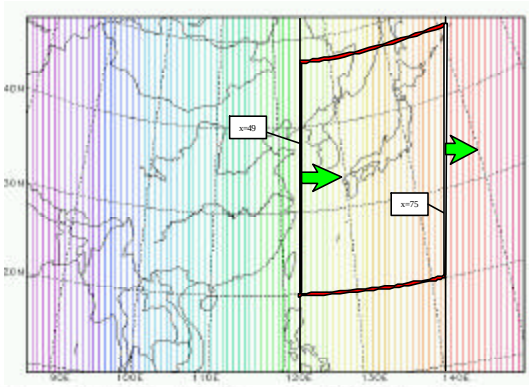

Cross Sections for Flux Calculations

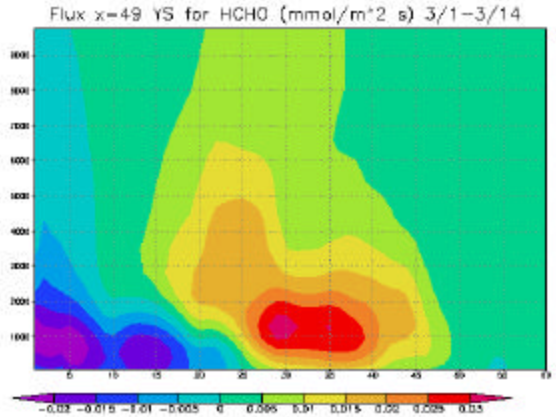

W E

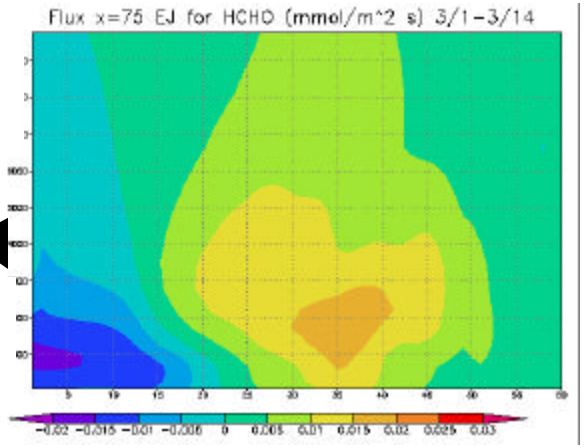

HCHO

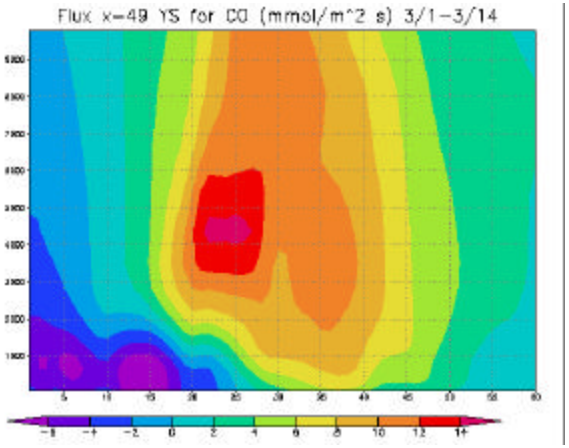

CO

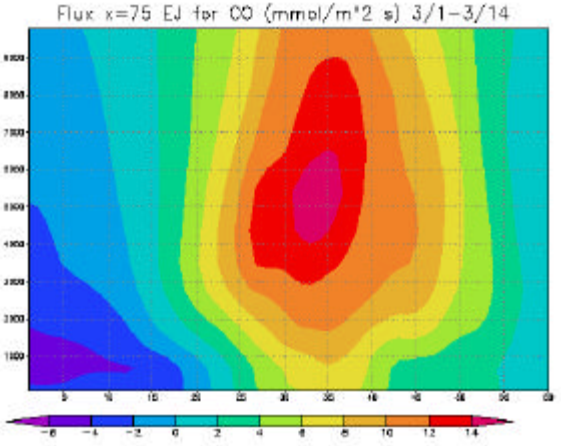

Figure 18

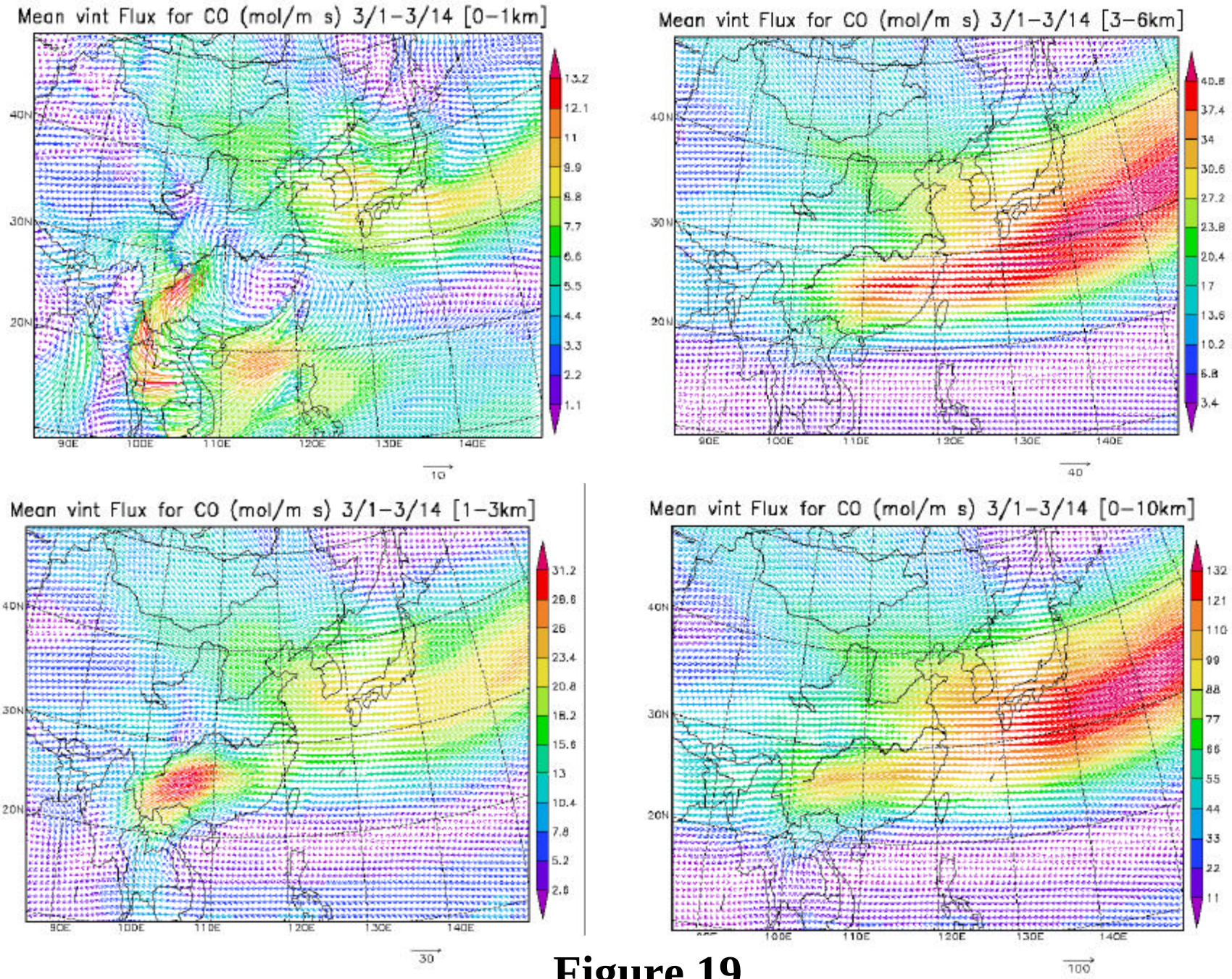
Mean vint Flux for CO (mol/m s) 3/1-3/14 [0-1km]
13.2
12.1
11
9.9
8.8
7.7
6.6
5.5
4.4
3.3
2.2
1.1
10
Mean vint Flux for CO (mol/m s) 3/1-3/14 [3-6km]
40.8
37.4
34
30.6
27.2
23.8
20.4
17
13.6
10.2
6.8
3.4
40
Mean vint Flux for CO (mol/m s) 3/1-3/14 [1-3km]
31.2
28.6
26
23.4
20.8
18.2
15.6
13
10.4
7.8
5.2
2.6
30
Mean vint Flux for CO (mol/m s) 3/1-3/14 [0-10km]
132
121
110
99
88
77
66
55
44
33
22
11
100

Figure 19

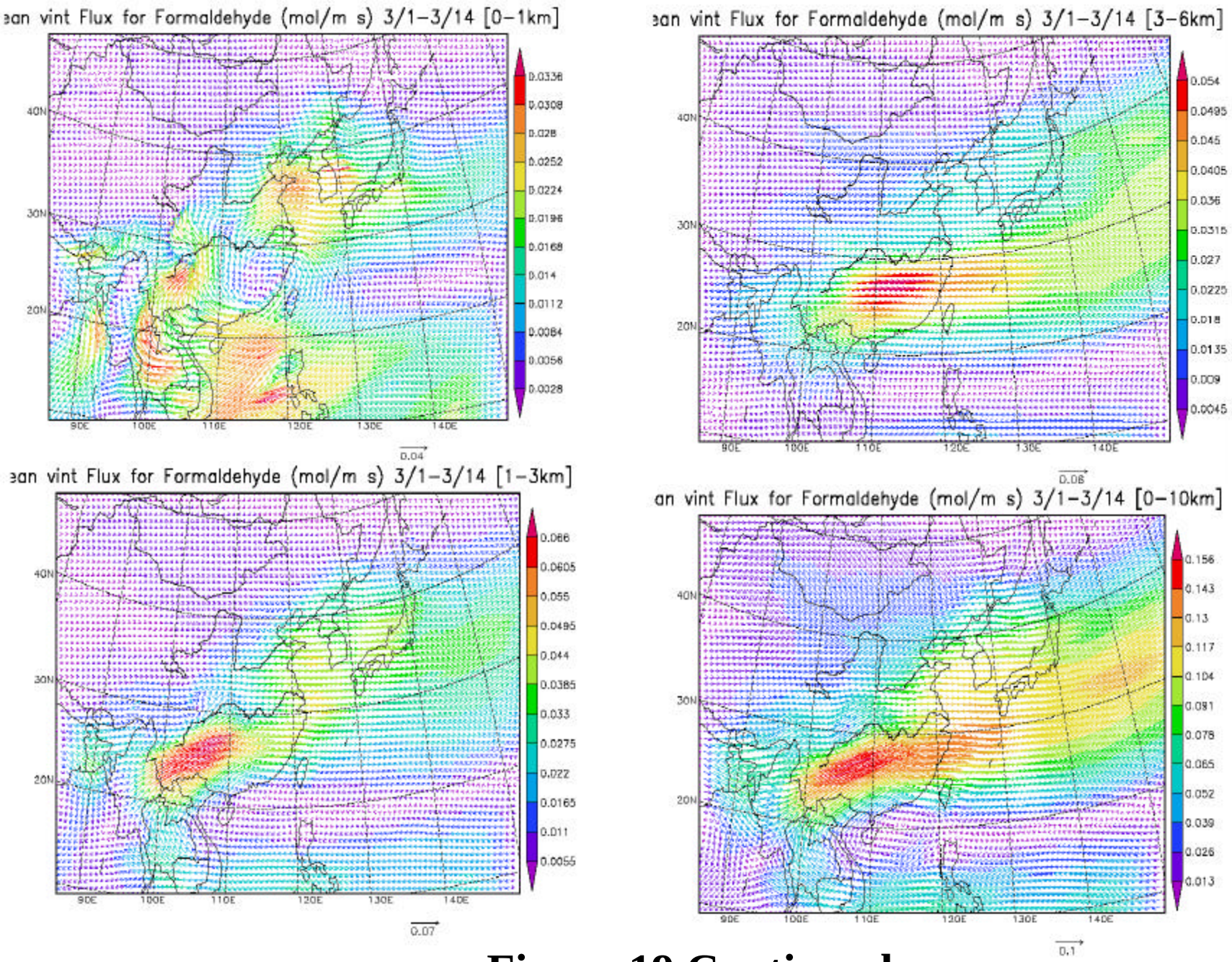

Figure 19 Continued

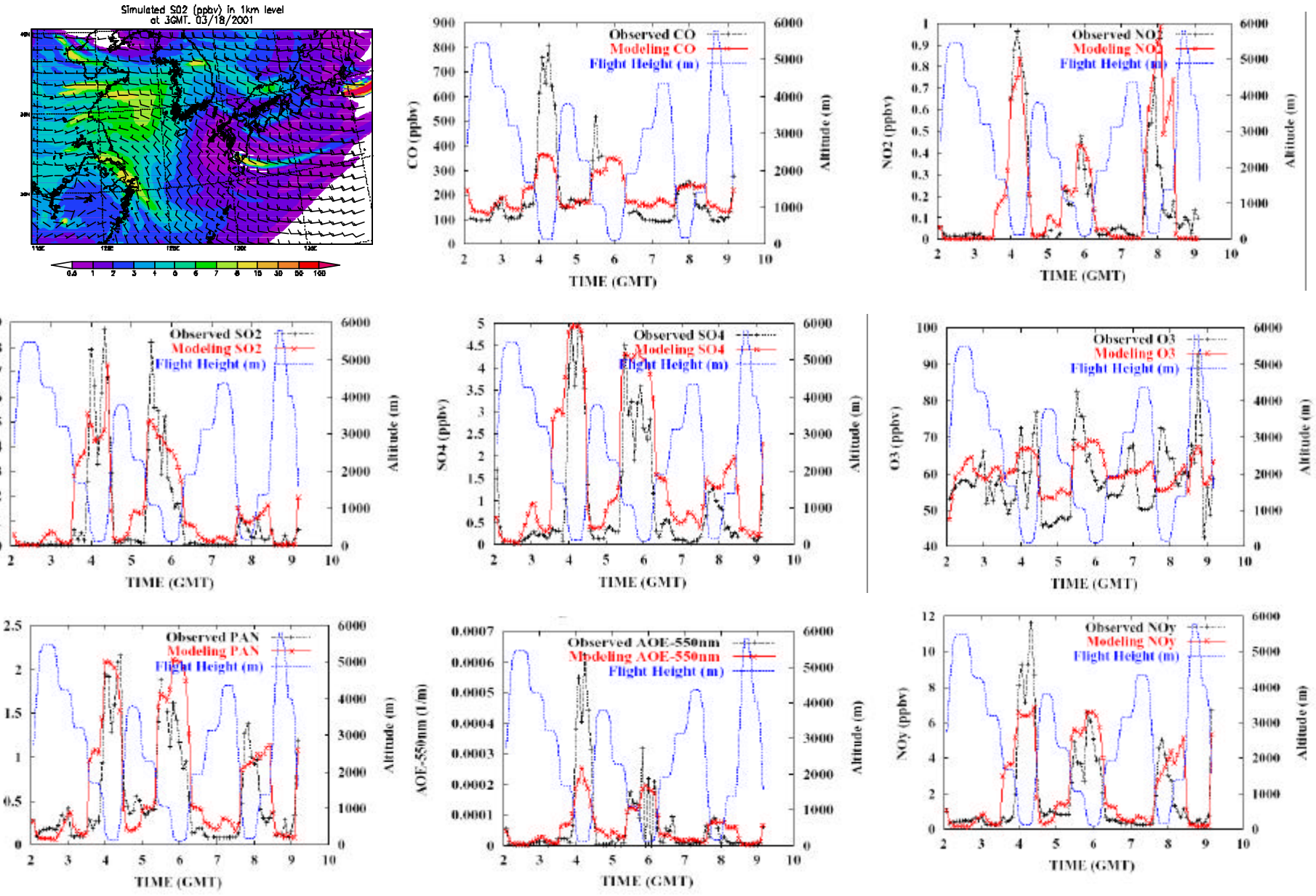
Simulated SO2 (ppbv) in 1km level
at 3GMT. 03/18/2001
Observed CO
Modeling CO
Flight Height (m)
CO (ppbv)
Altitude (m)
TIME (GMT)
Observed NO2
Modeling NO2
Flight Height (m)
NO2 (ppbv)
Observed SO2
Modeling SO2
Flight Height (m)
SO2 (ppbv)
Observed SO4
Modeling SO4
Flight Height (m)
SO4 (ppbv)
Observed O3
Modeling O3
Flight Height (m)
O3 (ppbv)
Observed PAN
Modeling PAN
Flight Height (m)
PAN (ppbv)
Observed AOE-550nm
Modeling AOE-550nm
Flight Height (m)
AOE-550nm (1/m)
Observed NOy
Modeling NOy
Flight Height (m)
NOy (ppbv)

Figure 20

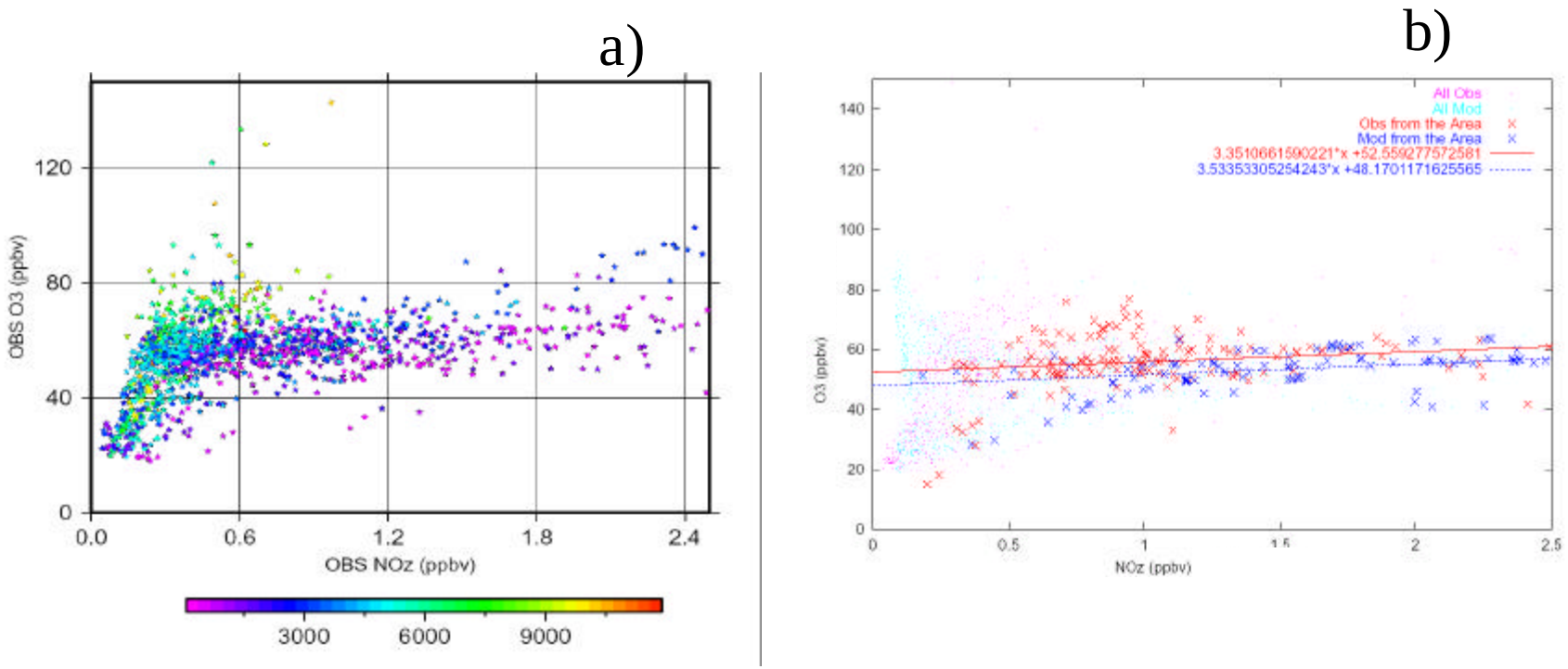
a)
b)
OBS O3 (ppbv)
OBS NOz (ppbv)
0
40
80
120
0.0
0.6
1.2
1.8
2.4
3000
6000
9000
All Obs
All Mod
Obs from the Area
Mod from the Area
3.3510661590221*x +52.559277572581
3.53353305254243*x +48.1701171625565
O3 (ppbv)
NOz (ppbv)
0
20
40
60
80
100
120
140
0
0.5
1
1.5
2
2.5

Figure 21

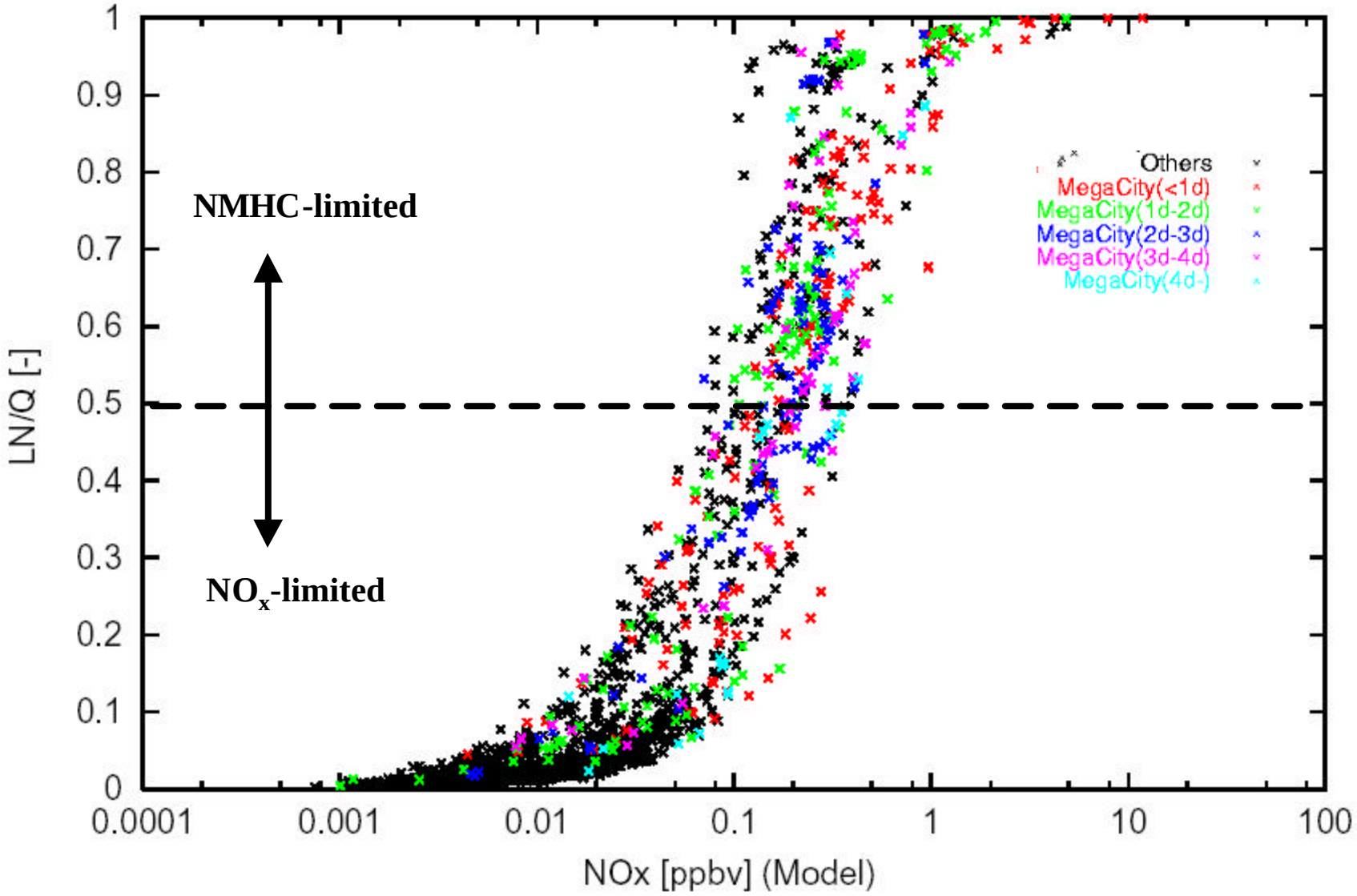
NMHC-limited
NOx-limited
LN/Q [-]
NOx [ppbv] (Model)
Others
MegaCity(<1d)
MegaCity(1d-2d)
MegaCity(2d-3d)
MegaCity(3d-4d)
MegaCity(4d-)
0
0.1
0.2
0.3
0.4
0.5
0.6
0.7
0.8
0.9
1
0.0001
0.001
0.01
0.1
1
10
100

Figure 22

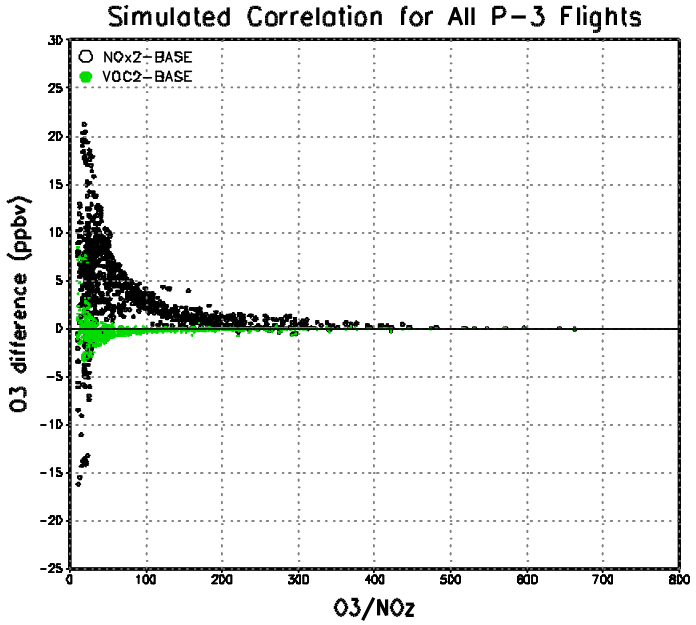
Simulated Correlation for All P-3 Flights
NOx2-BASE
VOC2-BASE
O3 difference (ppbv)
O3/NOz

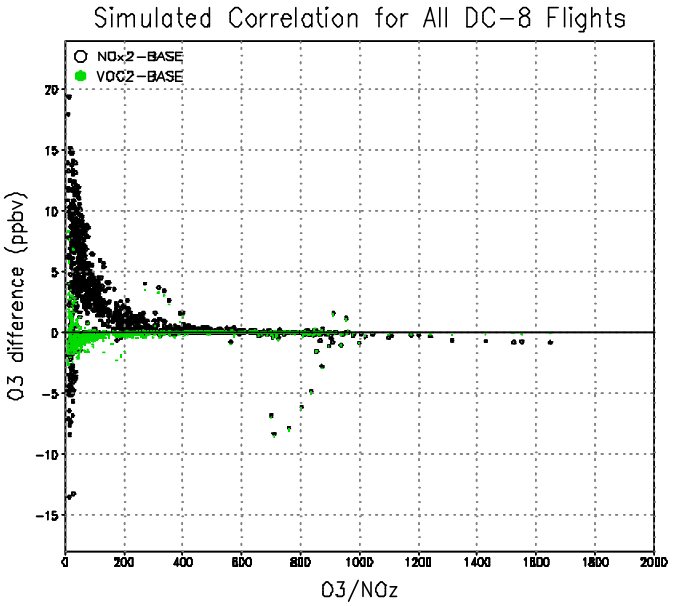
Simulated Correlation for All DC-8 Flights
NOx2-BASE
VOC2-BASE
O3 difference (ppbv)
O3/NOz

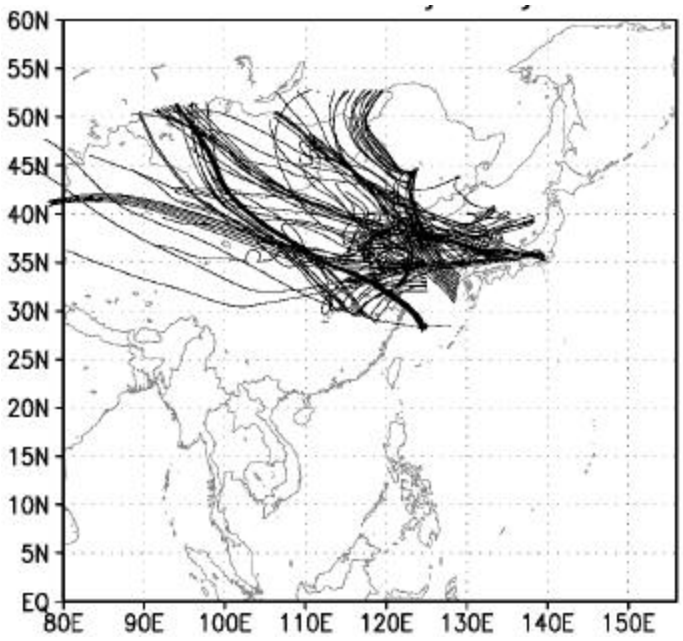
60N
55N
50N
45N
40N
35N
30N
25N
20N
15N
10N
5N
EQ
80E
90E
100E
110E
120E
130E
140E
150E

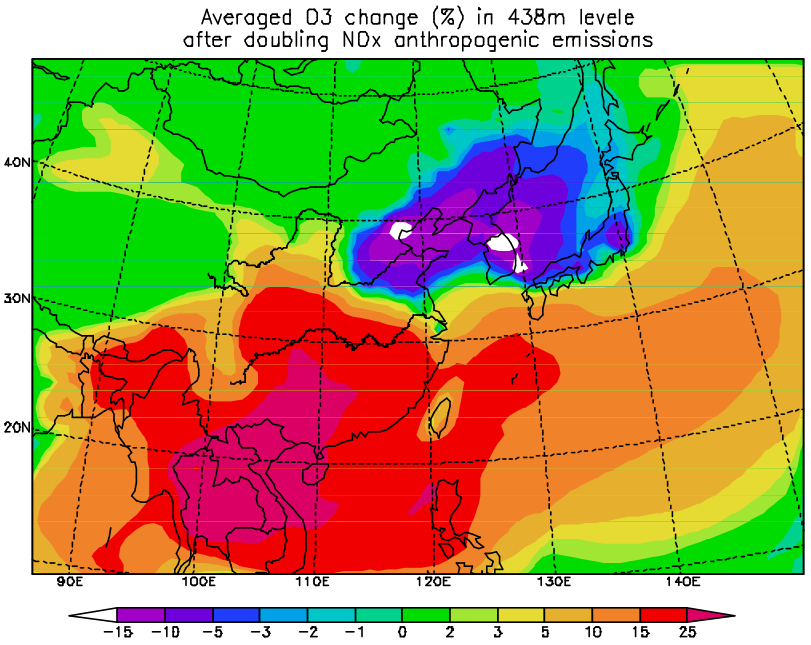
Averaged O3 change (%) in 438m levele
after doubling NOx anthropogenic emissions
40N
30N
20N
90E
100E
110E
120E
130E
140E
-15 -10 -5 -3 -2 -1 0 2 3 5 10 15 25

Figure 23